Chapter **1**

Introduction

Gamma-Ray Bursts (GRBs) can be counted as one of those rare serendipitous discoveries which have fascinated and embarrassed astronomers and astrophysicists for a long time, nearly four decades by now. Though a complete understanding still eludes us, interesting developments in our understanding of these explosions have occurred, thanks largely to several space missions: BATSE (Burst and Transient Source Experiment) on Compton Gamma-Ray Observatory, BeppoSAX, HETE II (High-Energy Transient Explorer), Swift and to the ground based multifrequency observations. On theoretical side, relativistic fireball model with several further generalisations has been the most successful.

In this chapter of the thesis, we give a brief introduction to GRBs (§ 1.1) and their afterglows (§ 1.2), starting from their properties inferred from observations. The distribution of energy output from Long GRBs is extremely narrow, (see § 1.3), which led to the inference that all of the Long GRBs, very likely, originate from a similar kind of progenitors, perhaps during collapse of a massive star. This comes as a strong support for the fireball model. A variety of GRB progenitors which are discussed in the literature are briefly discussed in § 1.4. We also discuss briefly about the central engines powering the GRBs (§ 1.5), their environments (§ 1.6) and GRB host galaxies (§ 1.7).

We have briefly introduced the fireball model, in § 1.8, and its dynamical evolution. The model assumes synchrotron radiation as the source of GRBs' brilliant multi-frequency display. We have introduced the commonly accepted radiation mechanism its spectrum for GRB afterglows and and derived important temporal scalings of the break frequencies. This leads us to simple general predictions about the behaviour of afterglow light curves.

After a few weeks time, the fireball enters a non-relativistic phase of evolution. Owing to different dynamical evolution, the evolution of the afterglow in this

phase is different. We have derived scalings for the afterglow evolution during the non-relativistic phase, as described in § 1.9.

The collimated outflows, or the jets, in GRBs were postulated to explain some observed deviations of the afterglow evolution. We have briefly discussed this evolution in § 1.10 and the resulting scalings were derived. An interesting and elegant model of structured outflows was introduced shortly afterwards to explain the narrow distribution of energy output from GRBs. This model assumes a quasi universal structure of energy distribution within the outflow. Thus the structured jets not only consider GRBs as a standard energy reservoir but also as a standard geometric configuration.

1.1   Gamma Ray Bursts

Gamma Ray Bursts (GRBs) were detected serendipitously by US satellites, Vela, which were launched to verify Soviet adherence to the Nuclear Test ban treaty forbidding outer space for the nuclear weapons test. It was soon realised that the bursts of γ-rays, lasting for 0.1 to 30 seconds, detected by the 'Vela' were not due to nuclear weapon detonations and were in fact coming from the outer space. They were not correlated with the known or expected sources of γ-rays - neither with the known supernovae nor with solar activity ! Klebesadel et al. (1973) determined that the GRB source positions did not include the Earth or the Sun. The GRBs were extra-solar system events.

The next major advancement in our understanding of these mysterious sources came gradually during the last decade of the last century. Burst and Transient Search Experiment (BATSE) aboard Compton Gamma Ray Observatory (C-GRO), which was functional during 1991-2000, detected a large number of GRBs -

2704 GRBs till 'Current Catalogue' (Paciesas et al., 1999; Paciesas, 2004) [1]. Each GRB has been uniquely numbered by the date of its detection at the Earth - GRByymmdd - where yy = last two digits of the year, mm = month, dd = day. If more than one GRB is detected in a day then a letter A, B... are appended to the names.

1.1.1   GRB distribution

Among the most important results from BATSE sample was the isotropic distribution of GRB events (Meegan et al., 1992) (See Figure 1.1) and their intensity distribution (Fishman et al., 1995) (See Figure 1.2 and Figure 1.3). The distribution of log(N)-log(Peak Flux) has a -3/2 power law slope at high fluxes (as would be expected for homogeneous distribution of sources in the Euclidean space) and shallower distribution at lower fluxes. Another test of source distribution viz. finding the average value of $\langle V/V_{max} \rangle$ where V and V_{max} are the volumes of the space enclosed by the source distance and the distace to which the source (of given intensity) could be detected, predicts that $\langle V/V_{max} \rangle = 1/2$, for homogeneous distribution of sources in Euclidean space. Instead, the results of this test showed that $\langle V/V_{max} \rangle < 1/2$. In summary, the intensity distributions show that the sources are not distributed homogeneously in the Euclidean space. These results are consistent with GRBs being cosmological events.

1.1.2   Classification

Common measures of the GRB duration, T_{90} is defined as a time within which 90% of the GRB counts arrive. The duration of GRBs has wide range - spanning over five orders of magnitude, ranging from less than 0.01 second to more than 100 seconds. The distribution of the GRB duration has a bimodal nature with first peak at about

---

[1]Electronic version is available at http://www.batse.msfc.nasa.gov/batse/grb/catalog/current/
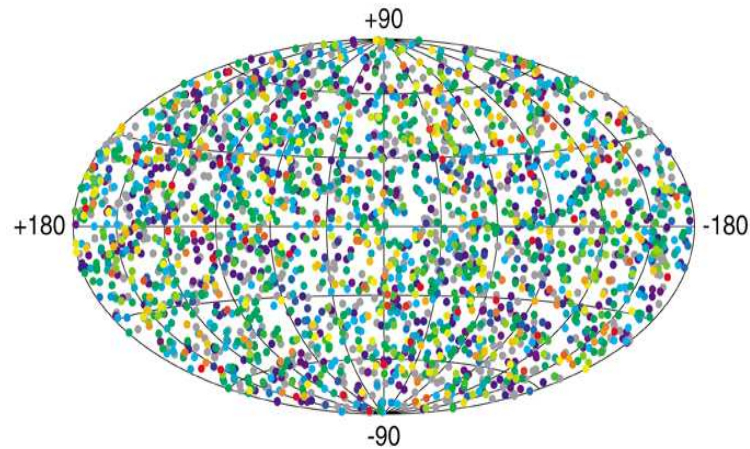
2704 BATSE Gamma-Ray Bursts

Figure 1.1: Distribution of 2704 GRBs detected by BATSE between 1991 and 2000. Their fairly uniform spread over the entire sky, indicated that they are either nearby and clustered around our position, or that they do not originate in our own Galaxy.

0.3 second and the second peak below 100 second (See Figure 1.4). A third peak at intermediate duration has been discussed in the literature but has a low significance.

Based on this distribution GRBs are classified into two categories - **Short GRBs** (SGRBs) with duration less than 2 seconds and **Long GRBs** (LGRBs) with duration greater than 2 seconds. Apart from the duration, it has also been found that the short GRBs have harder spectrum than the long GRBs. Based on these properties it has been inferred that the progenitors of the two classes of GRBs could be two different classes of objects. We discuss this point further in § 1.4

1.1.3 Burst Profile

The profile of the GRB light curves presents a rich diversity as a small sample shown in Figure 1.5 demonstrates. The GRB light curves also shows a variability, some times as short as of the order of a few milliseconds timescale. The burst spectra is of non-thermal nature and extends from $\sim$ 100 keV to $\sim$ MeV. The spectra are very
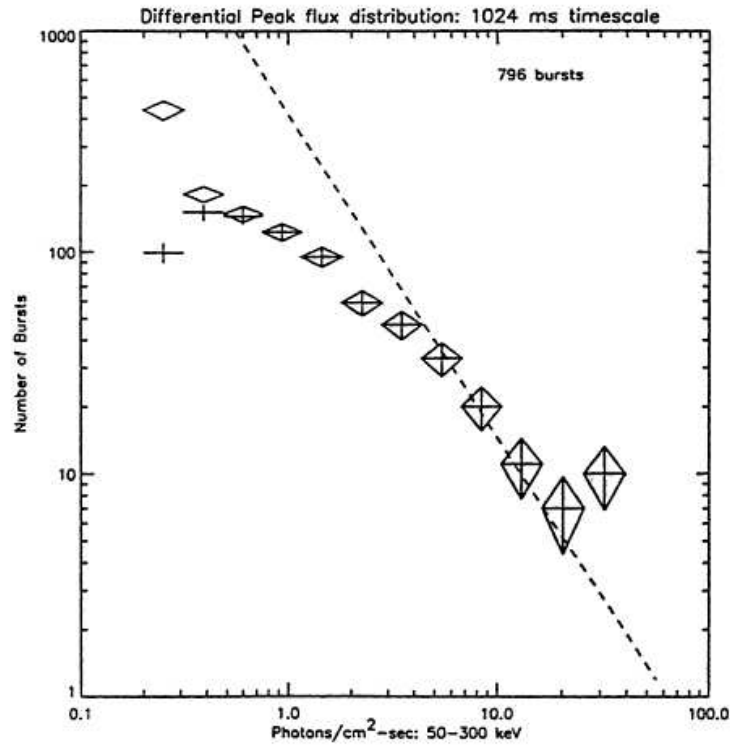
Figure 1.2: The peak flux distribution of 796 GRBs observed by BATSE. The flux is measured over 50-300 keV. This figure is taken from Fishman et al. (1995).

well described by Band function (Band et al., 1993) which is a broken power-law in energies joined smoothly at the break energy.

1.1.4   The Compactness Problem and The Relativistic motion

The millisecond timescale variability seen in the GRB light curves gives an important clue about relativistic motions involved in these explosions. The maximum size $(R \sim c\,\delta t)$ of the causally connected region, responsible for the short time variability (δt), turns out to be very small $(\sim 3000$ km for $\delta t \sim 10^{-2}$ s) and the resultant optical depth for pair production $(\tau_{\gamma\gamma})$ extremely large :

$$\tau_{\gamma\gamma} = f_{e^{\pm}} \frac{\sigma_T\ F\ (4\ \pi\ d_L^2)}{E_\gamma\ c^2\ \delta t} \tag{1.1}$$
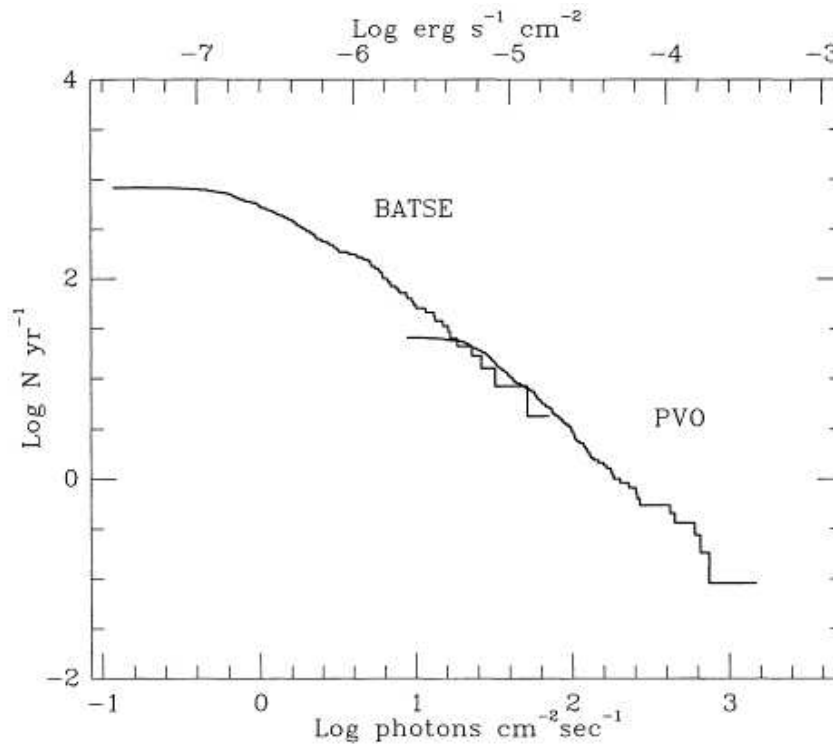
Figure 1.3: The log(N)-log(P) distribution with combined BATSE and Pioneer-Venus Orbiter (PVO) data. This figure is taken from Fishman et al. (1995).

where $f_{e^{\pm}}$ is a probability for photons to interact via pair production, F is the observed flux at a luminosity distance d_L, E_γ is the typical photon energy, σ_T is the Thomson scattering cross section and c is the speed of light. For typical values and cosmological distances $\tau_{\gamma\gamma} \sim 10^{15}$. Such a high value of $\tau_{\gamma\gamma}$ would highly suppress the production of high energy radiation and we would not be able to see the radiation from GRBs above pair production threshold. This is called as the 'Compactness Problem'.

However, in reality, that does not happen since we are able to detect high energy radiation from GRBs. The 'Compactness Problem' can be resolved if the radiating material is moving relativistically towards the observer. See Ruderman (1975) for the 'Compactness Problem' and Lithwick and Sari (2001) and references
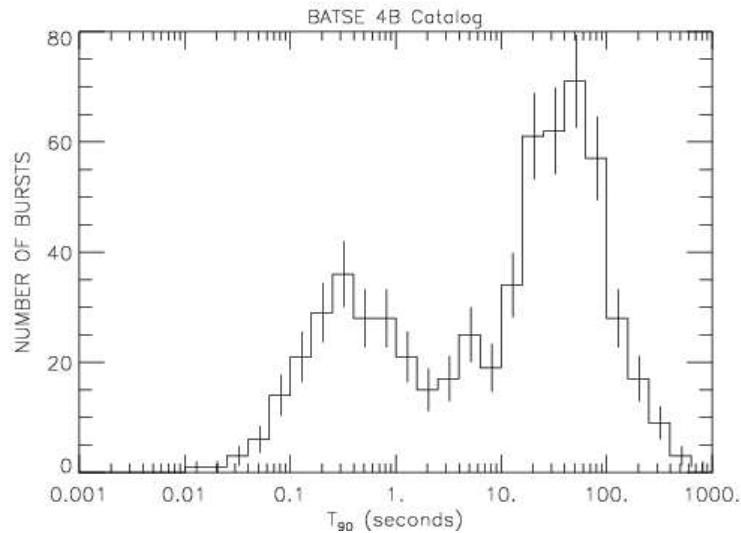
Figure 1.4: **GRB duration distribution :** GRBs clearly show a bimodal distribution of duration leading to the classification of GRB into Long GRBs and Short GRBs. See text for further discussion. This image is taken from Kouveliotou et al. (1993).

therein for refined solution of the 'Compactness Problem'. The relativistic corrections appear as follows :

1. The observed photons are blue shifted. Therefore, their energy in the rest frame of the emitting material is lower by a factor Γ - the bulk Lorentz factor of the emitting material and hence $f_{e^\pm}$ in Eqn (1.1) is lower.

2. The observed size of the source is $R = c\ \delta t\ \Gamma^2$ instead of previously inferred $R = c\ \delta t$.

Together this reduces the $\tau_{\gamma\gamma}$ by a factor Γ^{-6}. The fact that one observes the γ rays from GRBs imply $\Gamma \geq 100$. The relativistic motion of GRB outflows has subsequently been confirmed by direct radio observations (Waxman et al., 1998)
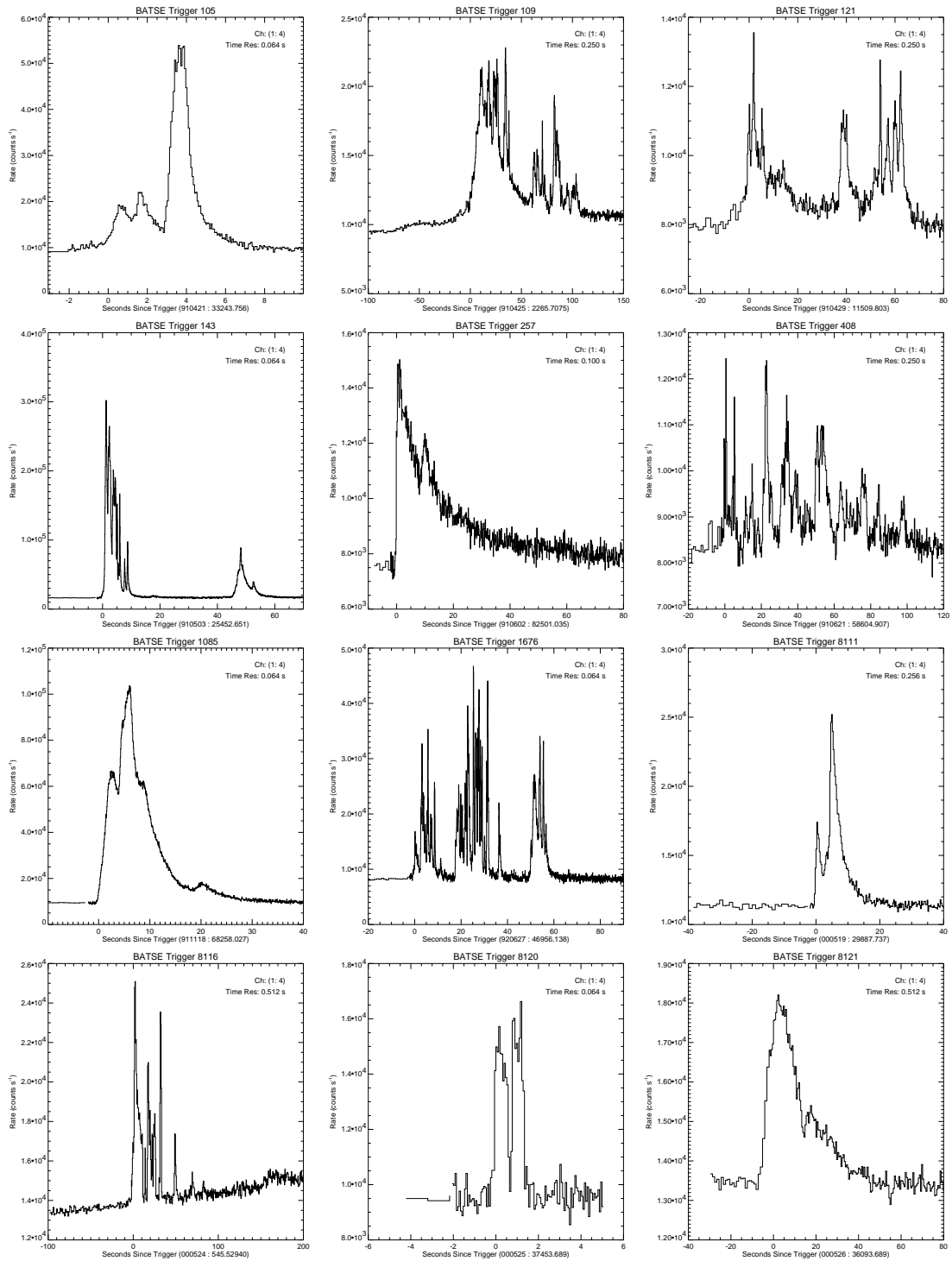
Figure 1.5: **Diversity of GRB light curves :** All the light curves are observed in BATSE's Channel 1-4 (> 20 keV). These light curves are taken from http://www.batse.msfc.nasa.gov/batse/grb/lightcurve/.

1.1.5   Short GRBs

While the afterglows of long GRBs are detected routinely, the situation is not that encouraging about short GRBs. Untill 2005, there was not a single SGRB with its afterglow detected. The situation changed with the launch of *Swift*. GRB 050509B was the first ever SGRB for which X-ray afterglow was detected. No optical transient was detected, but a nearby elliptical galaxy, with z = 0.225 has been attributed to it as its host galaxy. This was followed by a few more afterglows of SGRBs. Till the date, a total 15 SGRB afterglows have been discovered. However, some GRBs which do not qualify as SGRB because they last longer than 2 s, have also been classified as SGRBs due to various reasons. There are about 11 such SGRBs for which afterglows have been discovered. The first optical transient as well as a host galaxy (at z = 0.16) was identified for the SGRB 050709. The bright SGRB 050724 was the first whose radio afterglow was detected along with the X-ray and optical afterglows. This burst was also associated with an elliptical host galaxy. With a few secure redshifts of SGRBs, median redshift of SGRBs has been estimated to be z_{med} = 0.6, which is much lower than that of long GRBs. It should be noted though that the SGRB 060121 is estimated to be at $z \approx 4.6$.

One of the interesting features observed in the X-ray afterglows of SGRBs is 'flares'. The X-ray flares, discovered by *Swift* appear to be much more common in short GRBs than in long ones. GRB 050724, for instance, exhibited a strong flare at 5×10^4 seconds after the burst with about 10% of the prompt emission energy released during the flare.

Similar to the afterglows of long GRBs, the afterglows of SGRBs also show power-law decay behaviour. For two SGRBs jet breaks have also been inferred. With the known redshifts of nine SGRBs, it was found that the SGRBs are about 10 to 100 times less energetic than LGRBs. The amount of energy released in a few

SGRBs have been estimated to be $\sim 10^{49} - 10^{50}$ erg. For a recent review see Woosley and Bloom (2006).

The most popular model for short GRBs is the merger of compact stars, NS-NS or NS-BH. Recent discoveries show that the hosts of some SGRBs are nearby Elliptical Galaxies devoid of young stars as would be expected for compact star mergers. A larger sample in the future will confirm if this is indeed the case.

The sample of SGRBs with detected afterglows is still a very small sample to infer anything conclusively about them. The situation is expected to improve with further observations with *Swift* and the upcoming mission GLAST (Gamma Ray Large Area Space Telescope) along with a contribution from existing and upcoming robotic optical telescopes.

1.2   Afterglows

Understanding the physics of GRBs from the radiation received during the burst phase alone is a rather difficult task because the burst phase itself does not last long enough. Moreover, the occurrence of the bursts can not be predicted beforehand. In 1993, Paczynski and Rhoads (1993) predicted radio transients for GRBs. The major breakthrough in the study of GRBs came with the discovery of afterglow associated with the GRB 970228. The Dutch-Italian satellite BeppoSAX detected x-ray afterglow of GRB 970228 (Costa et al., 1997). The accurate position given by BeppoSAX allowed follow up and detection of optical afterglow (van Paradijs et al., 1997). The radio afterglow was detected for the first time for GRB 970508.[2]

The afterglow, as the word says, is the radiation that follows the main event,

---

[2]Visit following websites for a complete list of GRBs and related literature :
http://www.mpe.mpg.de/%7Ejcg/grbgen.html
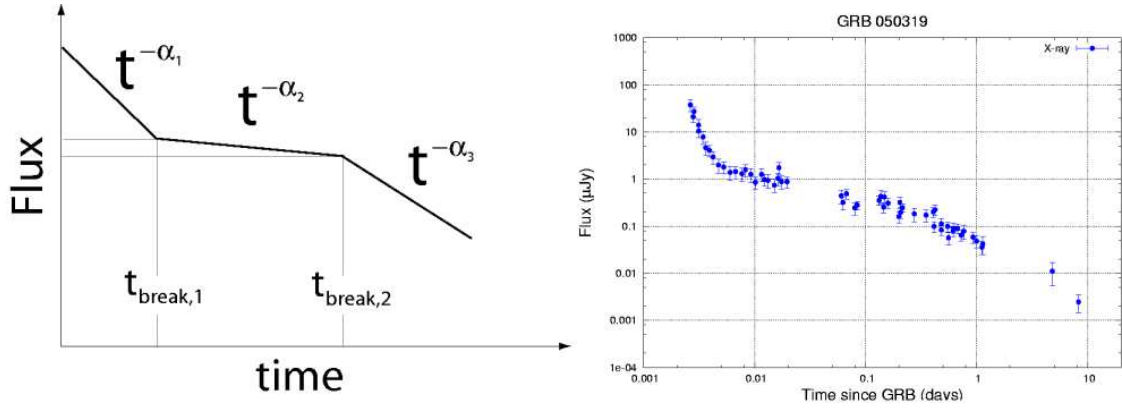http://grad40.as.utexas.edu/grblog.php

Figure 1.6: **X-ray afterglow lightcurve :** On the *left* is a schematic of the x-ray afterglow light curve of GRBs. The x-ray afterglows show three power-law segments joined by two breaks at typical times $t_{break,1} \sim 400$ s and $t_{break,2} \sim 0.5$ day after the burst. The decay of the afterglows typically has $\alpha_1 \sim 3$ to 5, $\alpha_2 \sim 0.6$ and $\alpha_3 < 2$. On the left is x-ray afterglow of GRB 050319 as observed by the x-ray telescope of *Swift*.

a GRB. The afterglows of many GRBs have been detected at all the frequencies from x-rays to radiowaves. The afterglows has a broken power-law spectrum. According to some accepted theoretical models, the afterglow is due to synchrotron radiation from the relativistic electrons. As a result, the afterglows in different spectral regimes (x-ray, optical and radio) give us information about different physical quantities such as the magnetic field, interstellar extinction, fireball dimensions etc. to mention a few. Even though the afterglow corresponds to a single physical effect we will broadly classify it into x-ray, optical and radio afterglow for discussion below. We will consider afterglows in quantitative detail at a later stage in § 1.8

1.2.1 X-ray Afterglows

More than 80 % of all of the GRBs exhibit x-ray afterglows. There are indications that the x-ray afterglow (XAG) begins very early, some times even while the burst is going on. The evolution of XAG can be described by a power-law (in fact, a broken

power-law) in frequency as well as in time : $f_\nu \propto \nu^{-\beta} t^{-\alpha}$, where f_ν is the observed flux and β and α are the spectral and temporal indices respectively. See Figure 1.6 and its caption for a schematic, an example and description. In some cases, flares have also been observed in XAGs.

The amount of energy released in XAG is about a few percentage of the total energy released in the burst. The XAGs are important to associate a transient with a GRB and to find its position accurately. The XAGs come from a part of the afterglow spectrum which is useful to constrain the magnetic field in which the radiating electrons are gyrating.

1.2.2 Optical Afterglows

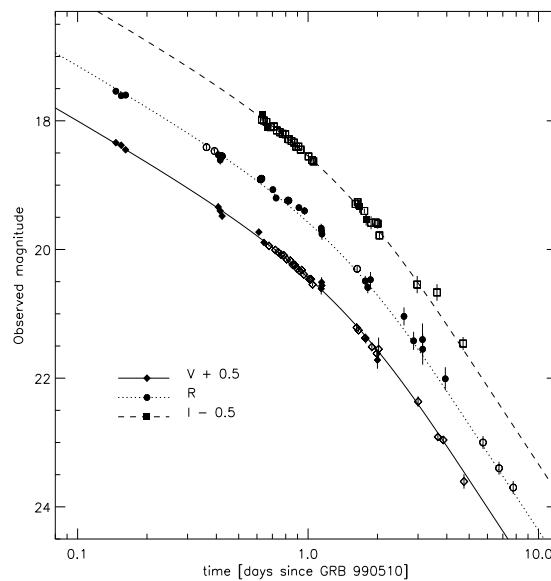Figure 1.7: **Optical afterglow lightcurve :** Optical afterglow of GRB 990510 in V, R and I bands. Many optical afterglows show a presence of an achromatic break as seen here. Theoretical models have interpreted such achromatic breaks as an effect of collimated outflow or jets (See § 1.10 for discussion on the Jets) from the GRB.

Optical afterglows (OAGs) have been detected for ∼ 50% of all the GRBs.

The OAGs are normally $\sim 19 - 20$ magnitude bright in R band when detected. Nowadays robotic telescopes routinely detect OAGs of GRBs as early as a few tens of seconds after the burst and in some cases even during the burst phase. The evolution of OAGs can also be described as a power-law (or a broken power-law). The light curves of some OAGs also show variations around the power-law decline. See Figure 1.7 and its caption.

The first redshift measurement for GRB 970508 (Metzger et al., 1997) established that the GRBs are at cosmological distances and hence made it possible to estimate the amount of energy released during the GRB for the first time. The OAGs are important to get accurate position of the afterglow which facilitates the detection of its host galaxy. They are also an important tool to study various other properties of the afterglow and of the interstellar material in the line of sight towards the GRBs.

1.2.3   Radio Afterglows

The rate of detection of radio afterglows (RAGs) is low (~ 10 %) compared to that of XAGs and OAGs and only a few of them have bright enough afterglows which can be followed up for a few days or months.

The self absorption frequency of the afterglow spectrum lies in the radiowave region. As a result, the RAG generally has a rising spectrum contrary to XAG and OAG spectrum. The evolution of the afterglow spectrum is such that the RAG is expected to keep rising during the initial few days and this has indeed been observed in many RAGs. This part of the spectrum (optically thick spectrum) is also useful to estimate the size of the emitting region. The RAGs exhibit fluctuations at early times and at high frequencies (> 4 GHz). It was suggested by Goodman (1997) that these fluctuations arise because of the interstellar scintillations and their evolution
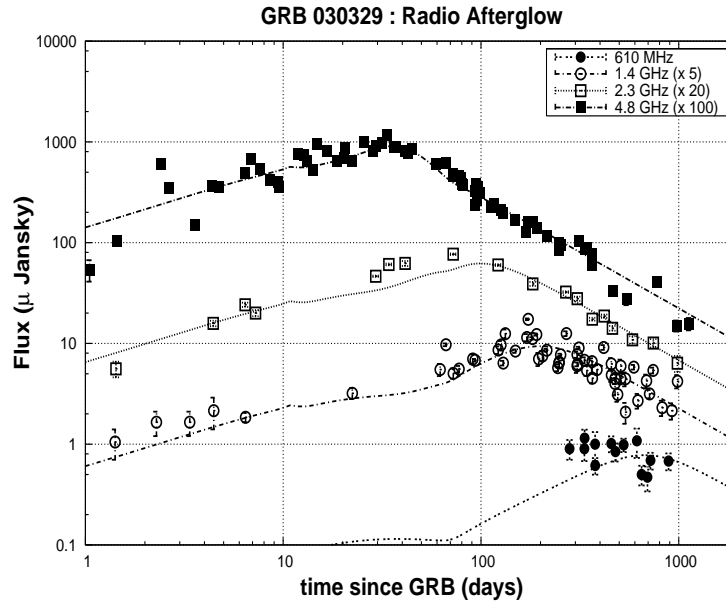
Figure 1.8: **Radio afterglow lightcurve :** Light curves of the radio afterglow of GRB 030329. In contrast with the x-ray (Figure 1.6) and optical (Figure 1.7) afterglow light curves which are usually seen decaying, the radio afterglow of many GRBs rises during first few days before declining. The lines plotted in this figure represent the light curves predicted using a model in which the GRB afterglow is due to synchrotron radiation emitted by shock accelerated electrons. The model and this afterglow is discussed in detail in Chapter 4.

was used to estimate the size of the emitting region (Frail et al., 1997). Bright RAGs which can be seen for a longer time allow observations of the afterglow when the blast wave has become non-relativistic. This provides a unique opportunity for unambiguous estimation of energy released into the blastwave. In Chapter 4, we will discuss the radio afterglow of GRB 030329, which we have followed for more than 1000 days, in detail.

1.2.4 Supernova Association

A peculiar supernova (SN) SN1998bw was found to be coinciding with the position of GRB 980425 reported by BeppoSAX (Galama et al., 1999). The optical afterglow

of GRB 980425 was never detected but the later observations done by XMM-Newton revealed that one of the sources in the BeppoSAX error box of the GRB position was indeed associated with SN 1998bw (Galama et al., 1999). It was for the first time that a SN was associated with a GRB, observationally. But it should be noted that long before SN 1998bw, theoreticans had indeed been associating GRBs with stellar deaths, though not exactly as SNs (Woosley, 1993).

SN 1998bw was an unusual SN of Type Ic, brighter than most of its kind with higher than usual ejection velocities and with energy budget larger by a factor about 10 compared to the rest. It is of interest to note that GRB 980425 which is associated with SN 1998bw was also of rare kind without a high energy component. GRB 980425 remains the nearest GRB to date, with measured redshift [3] of 0.0085. This implies an isotropic equivalent energy $\sim 10^{48}$ erg for GRB 980425 which is weaker by several orders of magnitude than a typical GRB [4].

A dramatic confirmation of the GRB-SN association, suspected from the GRB 980425-SN 1998bw case, came with detection of SN in the light curve and spectrum of a nearby GRB 030329 at a redshift $z = 0.1685$. The afterglow spectrum of GRB 030329 showed narrow emission lines and then broad peaks, characteristics of SN, developing after a few days. A 'Red Bump' seen in the afterglow light curve of GRB 030329 was interpreted as being due to the rising contribution of the SN in the afterglow brightness. SN 2003dh, the SN associated with GRB 030329, was similar to SN 1998bw in many respects. The amount of energy released in the explosion was estimated to be $\sim 5 \times 10^{49}$ erg, still significantly lower than most GRBs.

The observational evidence for GRB-SN association supports models [5]

---

[3]The redshift was measured for SN 1998bw. As we have noted before, optical afterglow of the GRB was never detected.

[4]See § 1.3 for more about GRB and afterglow energetics.

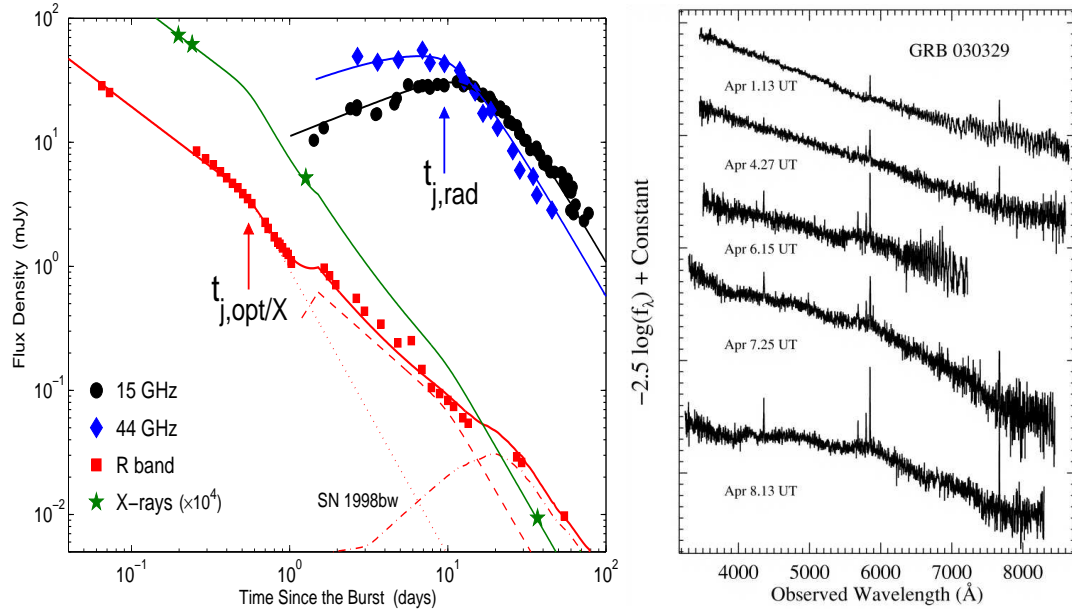[5]In particular, a model called the 'Collapsar model' of GRBs.

Figure 1.9: **GRB-SN association :** The afterglow light curve and spectrum of GRB
030329. The lines in the left panel are the afterglow light curves of GRB 030329 based on
the double jet model of Berger et al. (2003). The 'Red Bump', at ∼ 20 days, seen in the
afterglow light curve (*left* panel) is interpreted as being due to the underlying SN 2003dh.
The *right* panel shows evolution of the afterglow spectrum from continuum power-law at
early times to the narrow emission lines developing at later stages. The rise of the lines
and the broad peaks, characteristics of SNs, in the spectrum are temporally correlated with
the 'Red Bump' seen in the light curve. This confirms the association of the underlying
SN 2003dh with GRB 030329, both, photometrically as well as spectroscopically.

which assume that GRBs are produced during the collapse of a massive star. Sub-
sequently, a few more GRBs have been associated with SNs whose existence were
inferred from the 'Red Bumps' seen in the afterglow light curves. For a recent re-
view of GRB-SN association please refer to Woosley and Bloom (2006). The 'Red
Bumps' seen in the afterglows (e.g. see left panel of Figure 1.9) correspond to rise
in the brightness, presumably due to growing contribution of the underlying SN
light in the declining brightness of the afterglow, and transition to a much redder
spectrum. But it should be noted that a few other interpretations of the Red Bumps

do not require existence of underlysing SN (Esin and Blandford, 2000; Waxman and Draine, 2000).

1.2.5   Dark GRBs

Only ~ 50 % of the well localised GRBs show optical afterglows compared to x-ray afterglows for ~ 80 % of GRBs. Such GRBs without optical afterglows are called as 'Dark GRBs'. The absence of afterglows is not a result of poor sensitivity or late response of optical telescopes. A few afterglows of GRBs have indeed been found to be at least two magnitudes in R band fainter than average. The Dark GRBs, therefore, constitute a different class of objects. So far there have been three hypothesis put forward to explain the 'Dark GRBs' :

Large extinction : Dark GRBs are similar to other GRBs except that the line of sight towards them suffers from large extinction due to intervening absorbing material like large molecular clouds.

High redshift objects : Dark GRBs are similar to other GRBs but situated at a very high redshift ($z > 5$) so that the *Lyman break* is shifted to the optical band. However, a few optically faint afterglows, which could have been classified as Dark GRBs, for which redshifts have been measured did not have high redshifts.

Intrinsically faint : Optical afterglows of the Dark GRBs are intrinsically much fainter (2-3 magnitudes below) than that of other GRBs.

1.3   Energetics

With determination of the redshift for GRB 970508, it was possible to estimate the amount of energy released in the explosion in the form of radiation. Given the

observed fluence, f_ν, and redshift to a GRB, one can estimate the amount of energy emitted in γ rays assuming that the radiation was emitted isotropically. The E_γ^{iso} thus estimated for GRB 970508 was $\sim 10^{51}$ erg.

The redshifts of the GRBs are now routinely estimated either from the afterglow spectrum or from the spectrum of the host galaxy. The E_γ^{iso} estimated for many GRBs give alarmingly high values, $\sim 10^{54}$ erg in some cases. E_γ^{iso} assumes that the radiation was emitted isotropically, which may not be the reality and hence it may not be a good representation of the true amount of energy released during the burst. If the GRB outflow and hence the radiation is collimated instead of being isotropic then the actual amount of energy released is significantly less. For a typical opening angle of θ_{jet},

$$E_\gamma = (\frac{\Omega}{4\,\pi})\,E_\gamma^{iso} = \frac{[1 - cos(\theta_j)]}{2}\,E_\gamma^{iso} \qquad (1.2)$$

where Ω is the solid angle of collimation. Frail et al. (2001) finds that with this correction for collimation, the estimated E_γ is narrowly clustered around 10^{51} erg for GRBs. Bloom et al. (2003) has done a detailed study, including k-correction, of a number of GRBs and have estimated the amount of energy released in each one of them. They find that the $E_\gamma = 1.33 \times 10^{51}\;h_{65}^{-2}$ erg and a burst-to-burst variance about this value ~ 0.35 dex, a factor of 2.2. See Figure 1.10.

The amount of energy released during the afterglow phase, E_K, is estimated using the afterglow spectral parameters. Collimation corrected estimates of E_K are also found to be clustered around a similar value as E_γ.[6]

Another way of estimating the total amount of energy released in the burst is by using late time multi-frequency radio afterglow of GRBs. An advantage with

---

[6]Please note, E_γ and E_K are two different quantities. A fraction of the total amount of energy released during the explosion is emitted as γ radiation and this corresponds to E_γ. Another fraction is deposited in the 'GRB fireball' as kinetic energy (E_K) which drives the expansion of the 'fireball'. The total amount of energy released during the explosion is thus $E = E_\gamma + E_K$.
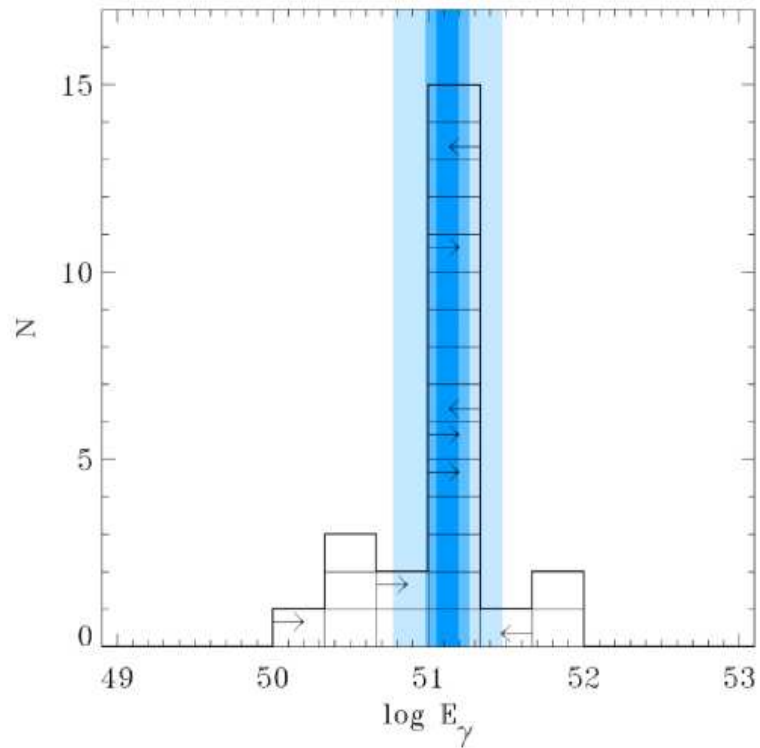
Figure 1.10: **GRB energy distribution :** Histogram of GRB energies E_γ with three equal logarithmic spacings per decade. The histogram shows a narrow distribution of GRB energies about the standard energy $E_\gamma = 1.33\ foe$, with an error of $\sigma = 0.07\ dex$ and rms spread is $0.35\ dex$ (a factor of 2.23) about this value. Bands of 1, 2, and 5 σ about the standard energy are shown. There are five identifiable outliers, which lie more than 5 σ from the mean. This image is taken from Bloom et al. (2003).

this method is that it does not suffer from the collimation uncertainties associated with the early optical and x-ray afterglows. We will discuss this method in detail in the chapter dealing with GRB 030329. The energy estimates using this method are consistent with $E_K \sim 10^{51}$ erg.

Recent observations indicate that the another class of GRBs - SGRBs - are less energetic compared to LGRBs by a few orders of magnitude. The amount of energy released in a few SGRBs have been estimated to be $\sim 10^{48}$ erg. For a recent review see Woosley and Bloom (2006).

1.4   Progenitors of GRBs

The amount and the time scale of energy release in GRBs put stringent constraints on the *progenitors*, the astrophysical objects one of whose evolutionary stages the GRBs could possibly be representing, and the *central engines* powering the GRBs. The GRBs are among the electromagnetically brightest known sources. The time scale of energy release is also incredibly small. It is also important to note that the GRBs are found at a wide range of cosmological distances (redshift range : 0.008 to 6.3). Taking this into account the models of GRB progenitors advocate massive star collapse or merger of compact binaries e.g. Neutron Star (NS) - Black Hole (BH) or NS-NS merger as the progenitors of GRBs.

Recent observations reveal that the locations of the LGRBs in their host galaxies coincide with star forming regions. Because massive stars end their life much faster than the less massive stars, their collapse at the end stages are very likely to be observed in the star forming regions. This supports the idea that the LGRBs are due to the collapse of massive stars.

Massive Wolf-Rayet (WF) stars are generally believed to be the progenitors of GRBs. The WFs have been found to be driving powerful winds during their life time which modify the circum-stellar material (CSM) density profile. If WFs are indeed causing the GRBs then the effects of modified CSM should be seen in the afterglow light curves. In chapter 6 we discuss a case where we indeed see such effect in the afterglow of GRB 050319. This further strengthen the claim that the massive stars are progenitors of GRBs.

The other class of GRB progenitors, compact star merger (NS-NS or NS-BH), is assumed to give rise to the Short GRBs (SGRBs). Recent discoveries show that the hosts of the SGRBs are nearby Elliptical Galaxies devoid of young stars as would be expected for the SGRBs. A larger sample in future will confirm if this is

indeed the case.

It should be noted that another class of mergers, merger of a NS and a White Dwarf (WD), has recently been proposed as a progenitor of GRBs, particularly LGRBs. For details see (King, 2006).

1.5   Central Engines powering the GRBs

A general feature of GRB central engine which is common in most of the models is accretion of a massive disk onto a compact object, most probably a newborn Black Hole. The observed short time scales can not be produced without compact objects and the amount of energy released requires a massive disk of at least 0.1 $M_\odot$. The generally accepted scenario − either collapse of a massive star or merger of compact stars − results in a black hole formation and an accretion disk around it. Accretion of this disk mass onto the BH lasts for several tens of seconds. Matter and radiation ejection in this process takes place along the rotation axis producing jets. In the case of collapsar model, if the jets are powerful enough they would bore through the stellar envelope. This is a distinct and important feature of the Collapsar Model. An important alternative model (Usov, 1992, 1994) considers Poynting flux driven by magnetic and rotational energies of a new born NS or magnetar.

Zhang and Mészáros (2001, 2002) have considered effects of a magnetar, as a central engine powering the GRB, on its afterglow. They consider a situation where the central engine remains active for several thousand seconds after the GRB and injects energy into the expanding fireball at a certain luminosity. A central engine injecting energy with luminosity $L \propto t^q$ can influence the fireball only if $q > -1$, in which case it results in the deceleration of relativistic shock wave at a slower rate. Using observed values of α and β of afterglow it should be possible to constrain the value of q. Shallow decays of some of the x-ray afterglows have been explained as

being due to the energy injection from the central engine. We will discuss this model in context of GRB 050401 in Chapter 5.

1.6 Environments of GRBs

Immediate environment of GRBs is of special interest as it can provide some clues about the progenitors of GRBs. The density profile of the material in the vicinity of the GRB progenitor, or the circum-burst material (CBM), is normally expected to be constant $[n(r) \propto r^0]$ or falling radially with distance : $n(r) \propto r^{-2}$. The later profile is also called as a wind-like density profile. Information about these density profiles could be obtained from the evolution of light curves of afterglows. The decay of the afterglow light curve is expected to be different if the CBM is uniformly distributed or if it is wind like. Variability seen in some of the afterglow light curves has been attributed to the clumpy CBM. Massive stars (e.g. Wolf-Rayet stars) drive powerful winds which modify the CBM to wind-like density profile. If GRBs are supposed to be the outcome of a collapse of such a massive star, then the afterglow is expected to show an evolution in a wind-like CBM. Interestingly, wind-like density profile has not been conclusively seen in most of the GRBs. Recently, we have interpreted the afterglow of GRB 050319 as being due to wind to constant density medium transition of CBM, a first ever detection of its kind. See Chapter 6. This supports the massive star collapse as the progenitor of GRBs.

1.7 GRB Hosts

In the *Swift* era, the host galaxies of a significant number of GRBs (~ 40) have been detected with reported magnitudes $20 < R < 30$. A few hosts have been detected in radio and millimeter bands also. While many researchers believe that the GRB hosts

are normal star forming galaxies, others argue that the GRB hosts are significantly bluer with star formation rate (SFR) much higher than the average. This is very important to know whether GRBs follow SFR and to which extent can they be used to determine the SFR at high redshift.

1.8   The Relativistic Fireball Model

A largely popular model of GRBs and afterglows, the Fireball model (Rees and Meszaros, 1992; Meszaros and Rees, 1993), provides a reasonable description of the phenomenon and the observations using simple assumptions. Essential features of the model can be summarised as follows. According to the fireball model, the afterglows [7] of GRBs are due to non-thermal synchrotron radiation emitted by shock accelerated electrons. This model assumes the explosion as a point explosion with a release of a large amount of energy $\sim 10^{52}$ erg and relatively low mass ejection. The large amount of energy released during the burst, drives a powerful relativistic shock wave which expands into the surrounding. The shockwave is an efficient way to convert bulk kinetic energy of the fireball into random (thermal) energy of the shocked material. As the shock wave propagates into the CBM, it sweeps up the matter and the shocked material is heated to high temperatures. A part of the bulk kinetic energy is also converted into the magnetic fields. The energy distribution of shocked electrons in the medium becomes a power-law $[n_e(\gamma)\ d\gamma \propto \gamma^{-p}\ d\gamma]$ with γ being Lorentz factor of the shocked electrons whose number density is n_e. These relativistic electrons gyrate in the post-shock magnetic field and emit synchrotron radiation which is seen as the afterglow of the GRB. The power-law distribution of

----

[7]Please note, the afterglows of GRBs were detected much after this model was proposed. The original article (Meszaros and Rees, 1993) predicted counterparts to the GRB radiation at other wavelengths which later on came to be known as the afterglows. At about a similar time, Paczynski and Rhoads (1993) independently predicted radio afterglows of GRBs.

the electron energies results in a power-law spectrum of the afterglow. The shock wave continues to decelerate as it propagates into the CBM. Assuming mass-energy conservation across the shock front, it has been shown that the Lorentz factor of the shock wave falls off as a power-law with the radius of the fireball. The temporal evolution of the shock wave is reflected in the afterglow spectral evolution and which in turn is responsible for the evolution of the afterglow light curves. A number of articles discuss this in detail e.g. Wijers and Galama (1999); Sari et al. (1998).

The GRB phenomenon is thus a relativistic analogue of another well known astrophysical explosion, the Supernova. Due to relativistic time dilation, introduced because of the high Lorentz factor of the shock wave, the GRBs & afterglows occur in a time scale much shorter than the SN.

1.8.1   Dynamics

1.8.1.1   Relativistic Shock and Conservation Equations

Shocks represent sharp discontinuity in the physical conditions such as the number density, temperature, pressure and the velocity of the material across the shock boundary. It turns out that the density, temperature and pressure across the shock have *self-similar* form. Such *self-similar* solutions in the case of non-relativistic shock are called Sedov-von Neumann-Taylor self-similar solutions. Their relativistic analogues have been derived by Blandford and McKee (1976) and are called as Blandford-McKee (BM) self-similar solutions. Conservation of mass, energy and momentum across the shock gives relations between certain quantities measured *upstream* and *downstream*. These are called as the *Rankine-Hugeniot* jump conditions. In the case of a relativistic shock wave, with Lorentz factor Γ_{sh}, the shock-jump conditions are obtained with the factors depending on Γ_{sh} as shown below.

$$n_2 \;=\; 4\,\Gamma\,n_1$$

$$e_2 \;=\; 4\,\Gamma^2\,n_1 m_p c^2 \tag{1.3}$$

$$\Gamma_{sh}^2 \;=\; 2\,\Gamma^2$$

where n and e are the number and the energy densities of the matter (measured in the local rest frame) respectively, with the subscripts 1 and 2 representing measurements *upstream* and *downstream*, respectively. The matter swept up by the relativistic shock wave clusters within a thin shell behind the shock front. Naturally, the compressed shocked material has the density, n_2, which is higher than that of the the unshocked material, n_1, as given by first of the above relations. This shocked matter coasts along with the shock front but with a Lorentz factor, Γ, which is lower than the shock Lorentz factor Γ_{sh} (See third of the above relations.). Shock jump conditions for non-relativistic shock wave are limiting cases of the relativistic shock-jump conditions with $\Gamma_{sh} \sim 1.0$.

$$n_2 \;=\; 4\,n_1$$

$$e_2 \;=\; 4\,n_1 m_p c^2 \tag{1.4}$$

1.8.1.2   Three Time Scales

While calculating the evolution of the relativistic fireball one has to be careful about the frame of reference of the measurement. There are three important frames of reference one can define for the case of explosion which involves relativistic motions of ejected material :

1. With respect to the centre of the explosion : $t = \int_0^R dr/c$, where r is the distance from the centre of explosion.

2. With respect to the ejected matter (i.e. co-moving with the ejected material) : $t_{co} = \int_0^R dr/(c\,\Gamma_{sh})$

3. With respect to the outside observer at rest with the CSM :

$$t_\oplus = (1 + z) \int_0^R dr/(c\Gamma_{sh}^2)$$

The definition of $t_\oplus$ here includes the cosmological time dilation factor $(1 + z)$ for a source at redshift z. Also, strictly speaking, the definition of $t_\oplus$ above is valid only for the material moving along the line of sight. The correct definition would involve projection of the radius along the line of sight, which we omit here for simplicity.

1.8.1.3   Fireball Expansion

The basic model for afterglow is a point explosion which generates a relativistic blast wave expanding into the CSM (Rees and Meszaros, 1992; Meszaros and Rees, 1993). For the case of GRBs, two important density profiles of the CSM are commonly considered, homogeneous density profile with $\rho = n\, m_p$ and wind density profile with $\rho = A\, r^{-2}$, for a constant mass loss rate $(\dot{M})$ and constant wind velocity (V_w). (By using $\dot{M} = 10^{-5}\, M_\odot\, yr^{-1}$ and $V_w = 1000\, km\, s^{-1}$, A can also be written down as $A = \frac{\dot{M}}{4\pi V_w} = 5 \times 10^{11}\, A_*$ gm cm^{-1}).

Below we consider a general density profile $\rho = A\, r^{-k}$. The results for the homogeneous and wind density profiles can be obtained by using $k = 0$ or $k = 2$, respectively. The evolution of the blast wave can be described by a self-similar solution. Blandford and McKee (1976) find a relation between the total energy (E), the Lorentz factor of the shock front Γ, the shock wave radius R and the density of the surrounding medium (represented here through A)

$$E = \frac{8\, \pi\, A\, \Gamma^2\, R^{3-k}\, c^2}{17 - 4k} \tag{1.5}$$

This equation is quite general and can be used for describing evolution of the shock wave if energy injection (see section 1.5) is also present. Here, we will consider $E \neq E(t)$ i.e. there is no energy injection or ejection [8]. Under such adiabatic evolution

---

[8]The energy losses by radiation are considered negligible.

of the fireball, we obtain a general result $R \propto \Gamma^{-2/(3-k)}$. Using third of the 'Three Time Scales' in section 1.8.1.2, this can be expressed in terms of a more important quantity, $t_\oplus$, the time in the observer's frame of reference. For a homogeneous density profile ($k = 0$) this gives,

$$R \quad \propto \quad E^{1/4} \, n^{-1/4} \, t_\oplus^{1/4}$$

$$\Gamma \quad \propto \quad E^{1/8} \, n^{-1/8} \, t_\oplus^{-3/8} \tag{1.6}$$

And for the wind density profile ($k = 2$) it results in,

$$R \quad \propto \quad E^{1/2} \, A^{-1/2} \, t_\oplus^{1/2}$$

$$\Gamma \quad \propto \quad E^{1/4} \, A^{-1/4} \, t_\oplus^{-1/4} \tag{1.7}$$

We are omitting the exact numerical co-efficients and will follow only the scalings for simplicity. For the numerical co-efficients, please refer to Wijers and Galama (1999) in the case of homogeneous and Chevalier and Li (2000) in the case of wind density profile.

1.8.2   Radiation

1.8.2.1   Electron Energy Distribution

It is normally assumed that the shocked electrons are accelerated to a power-law distribution of Lorentz factors,

$$n_e(\gamma_e) \, d\gamma = K_e \gamma_e^{-p} \, d\gamma_e \qquad \text{for } \gamma_m \leq \gamma_e \leq \gamma_u \tag{1.8}$$

starting with some minimum Lorentz factor γ_m and with a high energy cutoff corresponding to γ_u. The index of distribution p is usually determined from the observations and is commonly found to be $p \sim 2.3$ with a spread around this value. The value of γ_m and K_e can be found be using the the total energy in the electrons and

the total number of electrons.

$$\int_{\gamma_m}^{\gamma_u} n_e(\gamma_e)\, d\gamma_e \;=\; 4\,\Gamma\,n \tag{1.9}$$

$$\int_{\gamma_m}^{\gamma_u} \gamma_e\, m_e\, c^2\, n_e(\gamma_e)\, d\gamma_e \;=\; \epsilon_e 4\,\Gamma^2\, n\, m_p\, c^2 \tag{1.10}$$

The first equation is the conservation of total number of electrons in the power-law distribution and the second one is an expression that assumes that a fraction, ϵ_e, of the post-shock thermal energy goes into the electrons. Using equation 1.8, 1.9, 1.10 and a limit valid for all practical purposes $\gamma_u \gg \gamma_m$ one obtains

$$\gamma_m \;=\; \epsilon_e\, \frac{m_p}{m_e}\, \frac{p-2}{p-1}\, \Gamma \tag{1.11}$$

$$K_e \;=\; 4\,\Gamma\, n\, (p-1)\, \gamma_m^{p-1} \tag{1.12}$$

In general, ϵ_e can evolve with time. But given the available data sets of afterglows it is difficult to constrain the time variability of ϵ_e. Hence, in our entire discussion we will treat ϵ_e as a constant in time.

1.8.2.2   Post-Shock Magnetic Field

It is not clear in the case of GRBs, whether the magnetic fields are produced or the pre-existing magnetic fields are amplified. So it is perhaps a good starting point to assume that similar to ϵ_e a fraction, ϵ_B, of the post-shock thermal energy goes into the magnetic field.

$$\frac{B'^2}{8\pi} \;=\; \epsilon_B\, 4\,\Gamma^2\, n\, m_p\, c^2 \tag{1.13}$$

Primed quantities are measured in their local rest frame i.e. in the frame of shocked material. Similar to ϵ_e, in our entire discussion we will treat ϵ_B as a constant in time.

1.8.2.3   Synchrotron Spectrum of GRB Afterglow

Synchrotron process and spectrum is discussed in detail in various texts. See e.g. Rybicki and Lightman (1986). The power, $P(\nu, \gamma)$ initially rises as a power-law with

index $1/3$, reaches a peak at $v = 0.29\ v_{ch}$ and then declines as $P(v, \gamma) \propto e^{-(v/v_{ch})}\ \sqrt{v/v_{ch}}$. The spectrum is characterised by a frequency $v_{ch} \propto \gamma^2 B$. The synchrotron spectrum due to an assembly of electrons, in the case of afterglow, having a power-law energy distribution with index p (equation 1.8) turns out to be a power-law with index $\beta = (p-1)/2$ (see Equation 6.22a of Rybicki and Lightman (1986)). The power-law extends over a range of frequencies corresponding to γ_m and γ_u beyond which it has a different index. Below we discuss relevent spectral breaks and spectral slopes.

Spectral break due to minimum Lorentz factor γ_m

The power-law distribution of the electrons has a lower Lorentz factor cut-off which we identify as γ_m (See Equation 1.34). Characteristic synchrotron frequency corresponding to γ_m, is therefore, $v'_m \propto \gamma_m^2 B'$. More accurate expression for a characteristic synchrotron frequency involves dependence on pitch angle of electrons. Wijers and Galama (1999) simplify the picture by averaging the emission over electron distribution (and also over electron pitch angles) and define power due to an electron as 'an average power per electron'

$$P'_{v_m} = \phi_p \frac{\sqrt{3}\ q^3\ B'}{m_e\ c^2} \tag{1.14}$$

where

$$v'_m = \frac{3\ x_p}{4\ \pi}\ \frac{\gamma_m^2\ q\ B'}{m_e\ c} \tag{1.15}$$

As per the assumption of power-law electron distribution (Equation 1.8), there are no electrons in the distribution below γ_m. As a result, the spectrum below v_m is due to the superposition of spectral power due to rising part of the individual electron spectrum. Therefore, $P'_v \propto v^{1/3}$ for $v < v_m$.

Spectral break due to rapid cooling of high energy electrons

The above description of the spectrum is valid for those electrons which do not lose a significant fraction of its energy to radiation. Since the emitted power, $P_\nu \propto \gamma^2 B'^2$, the higher energy electrons, i.e. the electrons with higher Lorentz factor γ, lose more energy due to radiation and cool faster than those with lower Lorentz factor. One can then define a critical Lorentz factor (γ_c) and hence a corresponding critical synchrotron frequency (ν_c) above which cooling by synchrotron radiation is significant. The critical electron Lorentz factor γ_c is given by the condition $\Gamma \gamma_c m_e c^2 = P(\gamma_c)t$,

$$\gamma_c = \frac{6\pi m_e c}{\sigma_T \Gamma B^2 t} \tag{1.16}$$

where t refers to time in the frame of the observer. Characteristic frequency ν'_c can then be calculated using

$$\nu'_c = 0.286 \; \frac{3}{4\pi} \; \frac{\gamma_c^2 \; q \; B'}{m_e \; c} \tag{1.17}$$

The electron distribution given by Equation 1.8 is not valid for rapidly cooling electrons, and it can be shown that the new distribution has the following form

$$
\begin{aligned}
n_e(\gamma_e) \, d\gamma_e \;\; &\propto \;\; \gamma_e^{-p} \, d\gamma_e && \text{for } \gamma_m \leq \gamma_e \leq \gamma_c \\
&\propto \;\; \gamma_e^{-(p-1)} \, d\gamma_e && \text{for } \gamma_e \geq \gamma_c
\end{aligned}
\tag{1.18}
$$

resulting in a spectrum,

$$
\begin{aligned}
P'_\nu \;\; &\propto \;\; \nu'^{-(p-1)/2} && \text{for } \nu'_m < \nu' < \nu'_c \tag{1.19} \\
&\propto \;\; \nu'^{-p/2} && \text{for } \nu' > \nu'_c \tag{1.20}
\end{aligned}
$$

Spectral break due to synchrotron self absorption

We set synchrotron self absorption frequency where $\tau_\nu = \int_0^R \alpha_\nu \, dr = 1.0$. Using the shock thickness $\Delta r' \sim r/(4\gamma)$ and the self-absorption co-efficient, α_ν, as defined in

Rybicki and Lightman (1986) (their equation 6.52), we get

$$K_e \ B'^{(p+2)/2} \ \nu_a'^{-(p+4)/2} \ r = 1.0 \tag{1.21}$$

which can be inverted to get ν_a'.

Peak flux of the synchrotron spectrum

The peak of the spectrum can now be easily estimated using average power per electron at ν_m, which gives

$$F_{\nu_m}' = N_e P_{\nu_m}' \tag{1.22}$$

where N_e is the total number of radiating electrons. Transforming this to the observer at a luminosity distance d_L one gets

$$F_{\nu_m} = \frac{N_e \Gamma P_{\nu_m}'(1 + z)}{4\pi d_L^2} \tag{1.23}$$

Similarly, all the rest frame spectral breaks can also be transformed to the observer's frame of reference using $\nu_\oplus = \nu' \ \Gamma/(1 + z)$. The factor Γ blueshifts all the frequencies, as the radiating material is moving towards the observer with the Lorentz factor Γ. The factor $(1 + z)$, redshifts all the frequencies due to cosmological expansion. Using Equation 1.6 and 1.7 the final scalings of all the spectral breaks and flux, for homogeneous density profile of the CSM, becomes

$$\nu_{a\oplus} \propto t_\oplus^{-(3p+2)/[2(p+4)]}; \nu_{m\oplus} \propto t_\oplus^{-3/2}; \nu_{c\oplus} \propto t_\oplus^{-1/2}; F_{\nu_m\oplus} \propto t_\oplus^0 \tag{1.24}$$

Similarly, the scalings for wind density profile become

$$\nu_{a\oplus} \propto t_\oplus^{-[3(p+2)]/[2(p+4)]}; \nu_{m\oplus} \propto t_\oplus^{-3/2}; \nu_{c\oplus} \propto t_\oplus^{1/2}; F_{\nu_m\oplus} \propto t_\oplus^{-1} \tag{1.25}$$

These scalings are valid for a spectral regime $\nu_m \ll \nu_a \ll \nu_c$. The afterglow spectrum can now be divided into two different regimes, depending on whether $\gamma_m > \gamma_c$ or $\gamma_m < \gamma_c$. The case when $\gamma_m > \gamma_c$ is called as the *fast-cooling* and the case when $\gamma_c > \gamma_m$ is called as the *slow-cooling* The scaling of spectral breaks in those regimes are listed in Table 2.1.
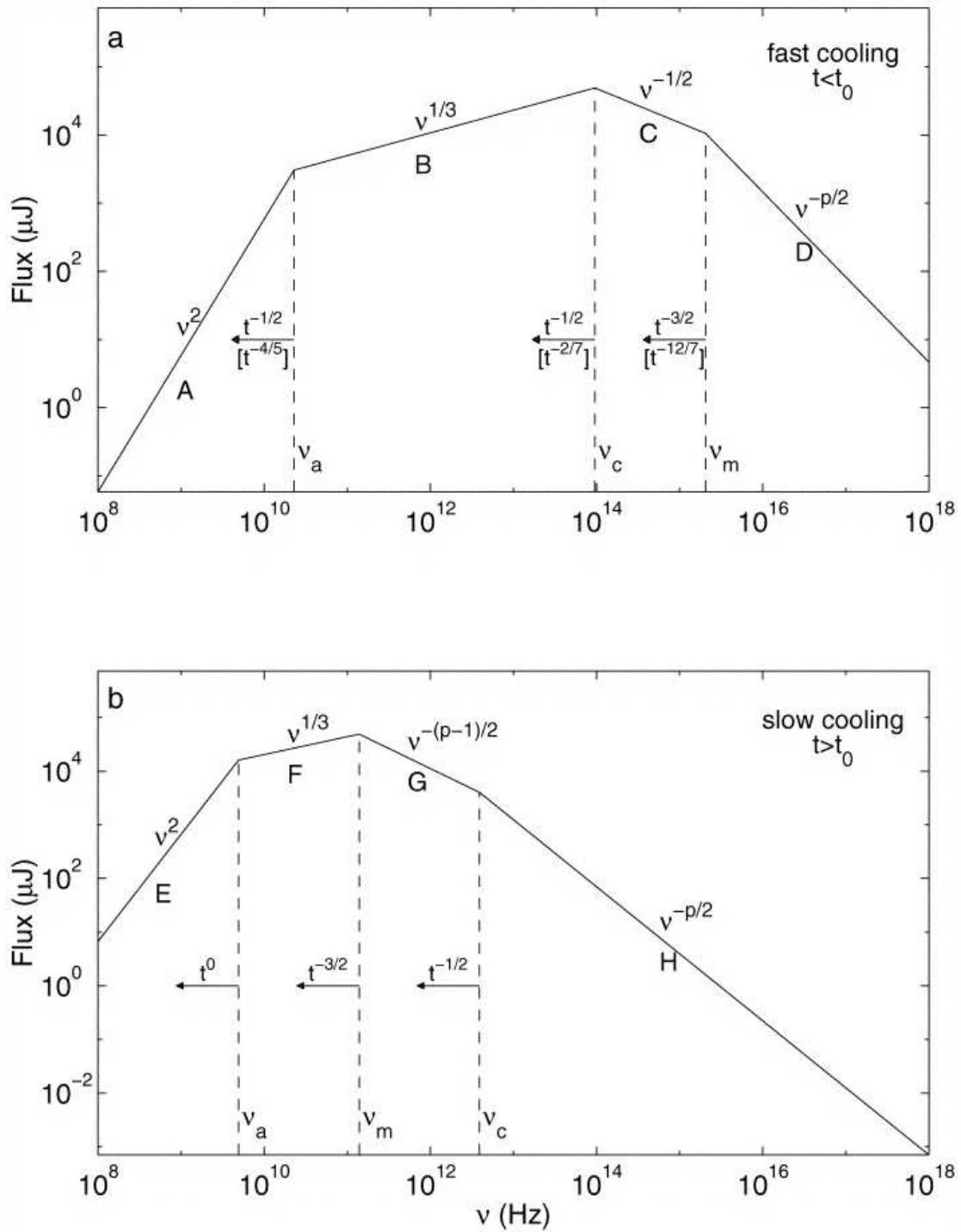
Figure 1.11: **The synchrotron spectrum of GRB afterglows :** The spectra of afterglow for typical values of spectral parameters during *fast cooling* (upper panel) and *slow cooling* (lower panel) phases. The frequencies, ν_m, ν_c, ν_a, decrease with time as indicated; the scalings above the arrows correspond to an adiabatic evolution, and the scalings below, in square brackets, to a fully radiative evolution. This figure is taken from Sari et al. (1998).

1.8.2.4   Afterglow Light curves

The afterglow light curve depends on how the break frequencies and the peak flux, F_{ν_m}, evolve with time. It also depends on the part of the spectrum where the frequency of observations, ν, is situated. The afterglow light curves at low frequencies (radio, milli-meter) and high frequencies (optical, x-ray) are plotted in Figure 1.12. For example, at the time of detection and subsequently the afterglow in optical and x-ray frequencies the light curves are seen declining (top panel in Figure 1.12). At radio frequencies the light curves are seen rising at early time, which then reaches a peak brightness and then declines (lower panel in Figure 1.12).

1.9   Non-Relativistic Evolution of the Fireball

The relativistic shockwave generated during the explosion (a GRB) encounters CSM and decelerates. After about a few days (in observer's frame of reference), when the shock wave has swept up a mass equivalent to the energy of explosion, the expansion of the shockwave decelerates to non-relativistic (NR) speeds. The radius and time of this transition to the NR expansion can be estimated as follows :

$$
\begin{aligned}
r_{NR} &= \left(\frac{3E}{4\pi\, n\, m_p\, c^2}\right)^{1/3} = 1.2\times10^{18}\,\frac{E_{52}}{n}\ \text{cm} \quad \text{for homogeneous density profile} \quad (1.26)\\
&= \frac{E}{4\pi A c^2} = 1.8\times10^{18}\,\frac{E_{52}}{A_*}\ \text{cm} \qquad\qquad \text{for wind density profile} \qquad (1.27)
\end{aligned}
$$

and

$$
t_{NR} = \frac{r_{NR}}{c} \sim 1.3\ \text{yr} \tag{1.28}
$$

where E_{52} is energy in units of 10^{52} erg. Here, we have assumed $E_{52} = 1$, and $n = 1$, a typical value for CSM.
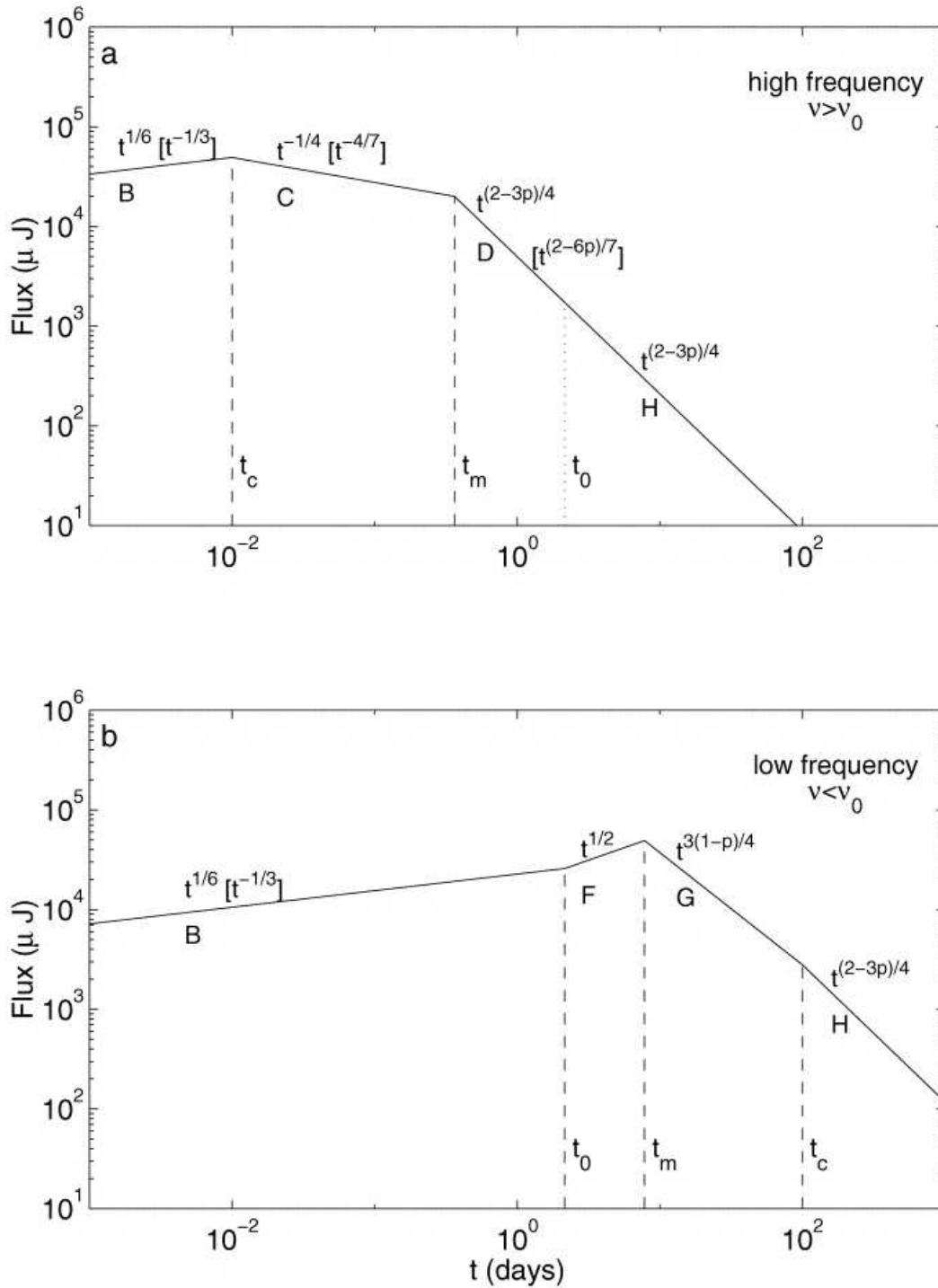
Figure 1.12: **The synchrotron light curve of GRB afterglows :** The light curves of afterglow expected at *higher frequencies* (upper panel) and at *lower frequencies* (lower panel) for typical values of spectral parameters. The vertical dashed lines corresponds to critical times : $t_c \Rightarrow$ epoch of $\nu = \nu_c$; $t_m \Rightarrow$ epoch of $\nu = \nu_m$; $t_0 \Rightarrow$ epoch of $\nu_m = \nu_c$ i.e. when the spectrum changes from *fast-cooling* to *slow-cooling* regime. ν is the frequency of observation. The scalings within square brackets are for radiative evolution which lasts only up to $t = t_0$ and the other scalings are for adiabatic evolution. This figure is taken from Sari et al. (1998).

1.9.1   Dynamics

1.9.1.1   Non-Relativistic Expansion of the Fireball

The expansion of the fireball obviously depends upon four parameters viz. E, r, A and t. Using the dimensional arguments it can easily be shown that $E \propto A \ r^{5-k} \ t^2$ with $\rho = A \ r^{-k}$ as before. This is equivalent to the Equation 1.5 and represents NR limit of the equation. Also, this indeed is a correct scaling as one obtains from the *Sedov-von Neumann-Taylor* (SNT) self similar solution for a non-relativistically expanding shock wave. The radius of the fireball can be obtained by inverting this :

$$
\begin{aligned}
r \quad &\propto \quad (\frac{E}{n})^{1/5} \ t_\oplus^{2/5} && \text{for homogeneous density profile} \\
&\propto \quad (\frac{E}{A_*})^{1/3} \ t_\oplus^{2/3} && \text{for wind density profile} \qquad (1.29)
\end{aligned}
$$

The speed of expansion can be obtained by differentiating Equation 1.29 :

$$
\begin{aligned}
\beta(t_\oplus) \quad &= \quad \beta_0 \ (\frac{t_\oplus}{t_0})^{-3/5} && \text{for homogeneous density profile} \\
&= \quad \beta_0 \ (\frac{t_\oplus}{t_0})^{-1/3} && \text{for wind density profile} \qquad (1.30)
\end{aligned}
$$

where $\beta(t_\oplus) = V_{sh}(t_\oplus)/c$ and $\beta_0 = \beta(t_\oplus = t_0)$. V_{sh} is the velocity of the shock-front.

The NR shock wave converts bulk kinetic energy of the incoming material into thermal energy of the shocked material :

$$
\begin{aligned}
U'_{thermal} \quad &= \quad \frac{1}{2} \ n_2 \ m_p V_2'^2 \\
&= \quad \frac{9}{8} \ n_1 \ m_p V_{sh}^2 \qquad (1.31)
\end{aligned}
$$

We have used one of the shock-jump conditions i.e. conservation of momentum across the shock boundary $n_2 \ V_2 = n_1 \ V_1$ and the fact that in the rest frame of the shocked fluid, the matter is coming in with a velocity $V_2' = (3/4) \ V_1$.

1.9.2   Radiation

1.9.2.1   Electron Energy Distribution

Even though the bulk velocity of the shock is NR, the thermal energy of the shocked material is very high and random velocities of the electrons are still relativistic. The energy distribution of electrons is still a non-thermal distribution as given by the Equation 1.8. The minimum Lorentz factor of the distribution can be estimated using relation similar to Equations 1.9 and 1.10 but this time by equating the left hand side of the equations with the $\epsilon_e \ U_{thermal}$.

$$\gamma_m \ = \ \epsilon_e \ \frac{9}{32} \ \frac{m_p}{m_e} \ \frac{p-2}{p-1} \ \beta^2 \tag{1.32}$$

$$K_e \ = \ 4 \ \Gamma \ n \ (p-1) \ \gamma_m^{p-1} \tag{1.33}$$

1.9.2.2   Post-Shock Magnetic Field

Assuming magnetic field of the shocked material is a fraction of its thermal energy gives

$$\frac{B'^2}{8\pi} \ = \ \epsilon_B \ \frac{9}{8} \ n \ m_p V_{sh}^2 \tag{1.34}$$

This can further be written down as simple scalings :

$$B' \ = \ B'_0 \ \beta \qquad \text{for homogeneous density profile}$$

$$= \ B'_0 \ r^{-1} \ \beta \qquad \text{for wind density profile} \tag{1.35}$$

1.9.2.3   Synchrotron Spectrum and Its Evolution

The synchrotron spectrum and evolution of the spectral breaks in the case of NR shockwave interacting with homogeneous CSM is discussed in Frail et al. (2000) and that with wind density profile is discussed in Chevalier and Li (2000). In this section, we will discuss these aspects of the afterglow and derive temporal scalings of the spectral breaks in various spectral regimes.

Spectral break due to minimum Lorentz factor γ_m

The characteristic synchrotron frequency corresponding to γ_m, is $\nu'_m \propto \gamma_m^2 B'$. Using Equation 1.15 and 1.32 one gets

$$
\begin{aligned}
\nu_{m\oplus} \quad &\propto \quad \beta^5 \propto t_\oplus^{-3} &\text{for homogeneous density profile} \\
&\propto \quad \frac{\beta^5}{r} \propto t_\oplus^{-7/3} &\text{for wind density profile}
\end{aligned}
\tag{1.36}
$$

Spectral break due to rapid cooling of high energy electrons

The critical electron Lorentz factor γ_c, above which the electrons loose larger energy due to radiation and cool faster is given by Equation 1.16. Because the post-shock magnetic field depends on $\beta(t_\oplus)$, the temporal evolution of γ_c and hence of corresponding frequency, $\nu_c \propto \gamma_c^2 B'$, is different from the that in the relativistic case. Using Equation 1.16, 1.17, 1.35 and 1.30, we find

$$
\begin{aligned}
\nu_{c\oplus} \quad &\propto \quad \beta^{-3} t_\oplus^{-2} \propto t_\oplus^{-1/5} &\text{for homogeneous density profile} \\
&\propto \quad \beta^{-3} t_\oplus^{-2} \propto t_\oplus^{1} &\text{for wind density profile}
\end{aligned}
\tag{1.37}
$$

As discussed in 1.8.2.3 the electron distribution given by Equation 1.8 will not be valid for rapidly cooling electrons. The new distribution will be similar to that in the case of relativistic expansion of the fireball and is given by Equation 1.18.

Spectral break due to synchrotron self absorption

Using the shock thickness $\Delta r' \sim r$ the optical depth can be approximated as, $\tau_\nu \sim \alpha_\nu r$. We set synchrotron self absorption frequency, ν_a at $\tau_\nu = 1.0$. Using the self-absorption co-efficient, α_ν, as defined in Rybicki and Lightman (1986) (their Equation 6.52), we get

$$
K_e \, B'^{(p+2)/2} \, \nu_a'^{-(p+4)/2} \, r = 1.0
\tag{1.38}
$$

We inverted this equation and used Equation 1.29, 1.12 and 1.35 to get temporal evolution of ν_a

$$\nu_{a\oplus} \propto t_\oplus^{\frac{-3(p-2/3)}{(p+4)}} \qquad \text{for homogeneous density profile}$$

$$\propto t_\oplus^{\frac{-(7p+6)}{3(p+4)}} \qquad \text{for wind density profile} \qquad (1.39)$$

Peak flux of the synchrotron spectrum

The peak of the spectrum can be estimated using Equation 1.23 with a non-relativistic limit $\Gamma \to 1.0$. Thus effectively $F_{\nu_m} \propto N_e B'$. Using Equation 1.35

$$F_{\nu_{m\oplus}} \propto t_\oplus^{3/5} \qquad \text{for homogeneous density profile}$$

$$\propto t_\oplus^{-1/3} \qquad \text{for wind density profile} \qquad (1.40)$$

The shape of the synchrotron spectrum, which essentially comes from the energy distribution of electrons (Equation 1.8), remains same as that in the relativistic expansion phase of the fireball. The final scalings of all the spectral breaks and flux, for homogeneous density profile of the CSM becomes

$$\nu_{a\oplus} \propto t_\oplus^{6/5} \ (\nu_a \ll \nu_m); \nu_{a\oplus} \propto t_\oplus^{\frac{-3(p-2/3)}{(p+4)}} \ (\nu_m \ll \nu_a); \nu_{m\oplus} \propto t_\oplus^{-3}; \nu_{c\oplus} \propto t_\oplus^{-1/5}; F_{\nu_{m\oplus}} \propto t_\oplus^{3/5} \quad (1.41)$$

Similarly, the scalings for wind density profile become

$$\nu_{a\oplus} \propto t_\oplus^{-2/15} \ (\nu_a \ll \nu_m); \nu_{a\oplus} \propto t_\oplus^{\frac{-(7p+6)}{3(p+4)}} \ (\nu_m \ll \nu_a); \nu_{m\oplus} \propto t_\oplus^{-7/3}; \nu_{c\oplus} \propto t_\oplus^{1}; F_{\nu_{m\oplus}} \propto t_\oplus^{-1/3} \quad (1.42)$$

1.10   Collimated outflows or Jets from GRBs

So far we have discussed isotropic outflows from GRBs and their evolution. But there are evidences that GRBs, instead of being isotropic, could be collimated. Some features observed in the light curves of afterglows are easy to explain using the assumption that the afterglow is due to collimated outflow or jets from the

GRB. It then becomes important to know the geometrical configuration of the jet and relative orientation of observer with respect to the jets. This understanding is essential to understand the burst mechanisms and the true event rates.

Soon after the discovery of afterglows in 1997, a few afterglows showed deviations from expected evolution. Optical light curves of a few GRBs showed presence of achromatic breaks – i.e. the breaks which are simultaneous in all wavebands – which could not be explained by using the assumption of isotropic fireball model or by using the evolution of spectral breaks. More natural explanation of the achromatic breaks is of dynamical origin : significant lateral expansion of initially collimated outflow.

It may be noted here that there are two different beaming effects one comes across in GRBs : One is the geometric beaming, or just the jet opening angle, θ_j of the outflow. Another is the well known relativistic beaming i.e. a cone of emission due to the relativistic motion of the emitting charge ($\theta \sim 1/\Gamma$), where Γ is the Lorentz factor of the emitting charge. Consider an initially relativistic collimated outflow from a GRB with $1/\Gamma < \theta_j$. In this case, an observer within an angle θ_j from the jet axis receives radiation only from $\theta \sim 1/\Gamma$ around the line of sight i.e. initially the observer does not receive radiation from the entire jet. As the outflow slows down and Γ falls, the observer receives radiation from a larger cone. Thus the observer has no knowledge about the radiation outside the relativistic beam of angle θ and the afterglow evolution for him is equivalent to the case of isotropic emission. Eventually, when $1/\Gamma \sim \theta_j$ two important effects take place. First, the observer starts to feel a deficit of energy per solid angle. Second, collimated outflow starts expanding sideways. Both these effects, which take place near simultaneously, can cause a break in the afterglow light curves.

There are two important models of the GRB jets which have extensively

been discussed in the literature :

Uniform Jets : This model assumes that the GRB outflow is confined within a cone with a uniform energy distribution and sharp boundaries (Rhoads, 1997; Panaitescu et al., 1998; Rhoads, 1999) We discuss this model in detail in § 1.10.1.

Structured Jets : This model assumes a quasi-universal jet structure, i.e., instead of sharp boundaries it uses angular energy distribution which falls rapidly away from the jet axis (more accurately, the jet axis is considered as the direction in which the angular energy peaks). We discuss this model in detail below in § 1.10.2.

1.10.1   Uniform Jets

Apart from the uniform energy distribution within the cone and sharp boundaries as assumed by the Uniform Jet model it also assumes that the observer is always along the line of sight. It predicts that the observed break time of the achromatic break is related with the opening angle of the jet. Although, this assumption seems contrived, it produces interesting results such as the collimation corrected energy turns out to be essentially a constant.

1.10.1.1   Dynamical Evolution

Relativistic Shock and Sideways expansion

Consider a situation in which the matter ejected during the explosion is collimated in a cone of half opening angle θ_j. Even though the matter is collimated and is moving in a forward direction it continues to expand in lateral direction too. Thus, the lateral size of the collimation at a radius r is $\sim c_s\, t_{co} + r\, \theta_j$, where c_s is the speed of sound in the expanding medium with which the ejecta is moving in the lateral

direction. For a relativistic matter $c_s \approx c/\sqrt{3}$. The later term $(r\,\theta_j)$ dominates during early times and the lateral expansion of the material is not significant. However, at later times first term $(c_s\,t_{co})$ starts dominating and the effects of lateral expansion becomes important. The transition happens, as can be seen from the second of the 'Three Time Scales' at $\Gamma \sim 1/\theta_j$.

Fireball Expansion

Details of the fireball expansion in the case of Uniform Jets have been calculated by Rhoads (1999) for constant density medium. Chevalier and Li (2000) discuss the Uniform Jets in the case of wind density profile. It has been shown by Rhoads (1999) that once lateral spreading becomes dominant forward expansion of the fireball becomes extremely slow and can be approximated as halts. Hence, after the jet break, for wind and constant density profiles

$$R \propto t_\oplus^0 \tag{1.43}$$

Using third of the 'Three Time Scales' the temporal evolution of γ scales as

$$\Gamma \propto t_\oplus^{-1/2} \tag{1.44}$$

1.10.1.2   Radiation

As indicated by Equation 1.43, evolution of r is independent of the density profile of the external medium. Hence, evolution of the spectral breaks should be same for constant and wind density profiles.

Spectral breaks and their temporal evolution

Characteristic synchrotron frequency corresponding to γ_m, can be calculated as before. But because Γ is decaying faster after the jet break ν_m is also expected to decay faster. Using Equation 1.15, 1.11, 1.13 and 1.44 we determine ν_m and transform it

to the observer's frame of reference using $\nu_\oplus = \nu' \; \Gamma/(1+z)$ to get

$$\nu_{m\oplus} \propto t_\oplus^{-2} \tag{1.45}$$

Using Equation 1.16, 1.13, and 1.44 we determine the evolution of cooling frequency after the jet break and transform it to the observer frame to get

$$\nu_{c\oplus} \propto t_\oplus^0 \tag{1.46}$$

And similarly, using Equation 1.21, 1.43, and 1.44, we determine the evolution of self absorption frequency after the jet break and transform it to the observer frame to get

$$\nu_{a\oplus} \propto t_\oplus^{\frac{-2(p+1)}{(p+4)}} \tag{1.47}$$

The evolution of the peak of the spectrum can now be estimated using average power per electron at ν_m, which gives

$$F'_{\nu_m} = N_e P'_{\nu_m}$$
$$F_{\nu_m\oplus} \propto t_\oplus^{-1} \tag{1.48}$$

Afterglow Light curves

The afterglow light curves in different spectral regimes can be calculated using temporal evolution of break frequencies and of the peak of the spectrum. We have calculated and listed the expected spectral and temporal decay indices in Table 2.1. An important point to note here is that the afterglow light curves at frequencies higher than ν_m (if $\nu_m > \nu_a$) or higher than ν_a (if $\nu_m < \nu_a$) decay with $F_\nu \propto t_\oplus^{-p}$. Optical and x-ray frequencies almost always satisfy the condition $\nu > \nu_m, \nu_a$. As a result, after the jet break optical and x-ray light curves are expected to decay with index p making a direct determination of p possible.

The achromatic break seen in the optical light curves of GRB 990510 in Figure 1.7 in one of the early examples of breaks which have been interpreted as being due to the lateral spreading of the collimated ejecta i.e. the jet.

Criticism against the Uniform Jet model

The jet break time is directly related to the jet opening angle θ_j. Frail et al. (2001); Bloom et al. (2003) has estimated jet opening angles from achromatic breaks seen in a number of afterglows. The resultant distribution θ_j show a large dispersion. Similarly, distribution of E_{iso} also shows a large dispersion. But it turns out that the collimation corrected energy, $E_\gamma = E_{iso}\ (\theta_j^2/2)$, is essentially a constant. Based on this observation, Frail et al. (2001); Bloom et al. (2003) suggested a constant energy reservoir of energy $E_\gamma = 1.3 \times 10^{51}$ erg for GRBs. But this apparently elegant result then poses a further question : If there is universal energy reservoir, why are the GRBs collimated to different collimation angles.

1.10.2   Structured Jets

The Structured jet is an alternative model for jets in GRBs which not only considers GRBs as a standard energy reservoir but also as a standard geometric configuration. Apparent diversity in GRBs could be a result of different geometric configuration and/or of different observer-jet orientation. If this indeed is the case, then the structured jet model appears more elegant than the uniform jet model because it shows a possible way to understand the diversity of GRBs in a unified picture.

The structured jet assumes a non-uniform distribution of *Lorentz* factor and of energy per solid angle within the jet and the observer at a viewing angle θ_v away from the jet axis. To put it quantitatively,

$$\epsilon(\theta) \;=\; \epsilon_0\ (\frac{\theta}{\theta_c})^{-a}$$

$$\Gamma(\theta) \;=\; \Gamma_0 \, (\frac{\theta}{\theta_c})^{-b} \tag{1.49}$$

where $\epsilon(\theta)$ and $\Gamma(\theta)$ are the energy per unit solid angle and the *Lorentz* factor respectively which are dependent on the angle from the jet axis, θ. A small core of angle θ_c is introduced to avoid singularity at $\theta = 0$. Such configurations have earlier been discussed by Meszaros et al. (1998); Dai and Gou (2001); Rossi et al. (2002). In this model, achromatic break occurs when the *Lorentz* factor of material directed towards the observer falls below $1/\theta_v$, i.e. $\Gamma(\theta_v) \sim 1/\theta_v$, rather than $1/\theta_j$ as in the case of Uniform Jet model. In this way, different times of jet break in this model are due to different θ_v. However, it should be noted that the power-law model as assumed here is not necessary to reproduce the jet break effects. Similar results could be obtained even with non power-law energy distribution models such as Gaussian jet profile (Zhang and Mészáros, 2002a).

Granot and Kumar (2003) have investigated the effects that the structure of GRB jets has on the afterglow light curves for observers located at different viewing angles. They have considered the Lorentz factor and kinetic energy per unit solid angle to be power-laws of the angle from the jet axis initially.

$$
\begin{aligned}
\epsilon(\theta, t_0) &= \epsilon_0 \Theta^{-a} \\
\Gamma(\theta, t_0) &= 1 - (\Gamma_0 - 1)\Theta^{-b} \\
\Theta &= \sqrt{1 + (\frac{\theta}{\theta_c})^2}
\end{aligned}
\tag{1.50}
$$

The qualitative comparison between the resulting light curves and afterglow observations constrains the jet structure, with $a \approx 2$ and $0 \le b \le 1$. The resultant light curves for different combinations of a and b are shown in Figure 1.13.

Prediction of Structured Jet Models

A structured jet model makes several predictions which can be tested with observations. Below we list a few of them briefly :
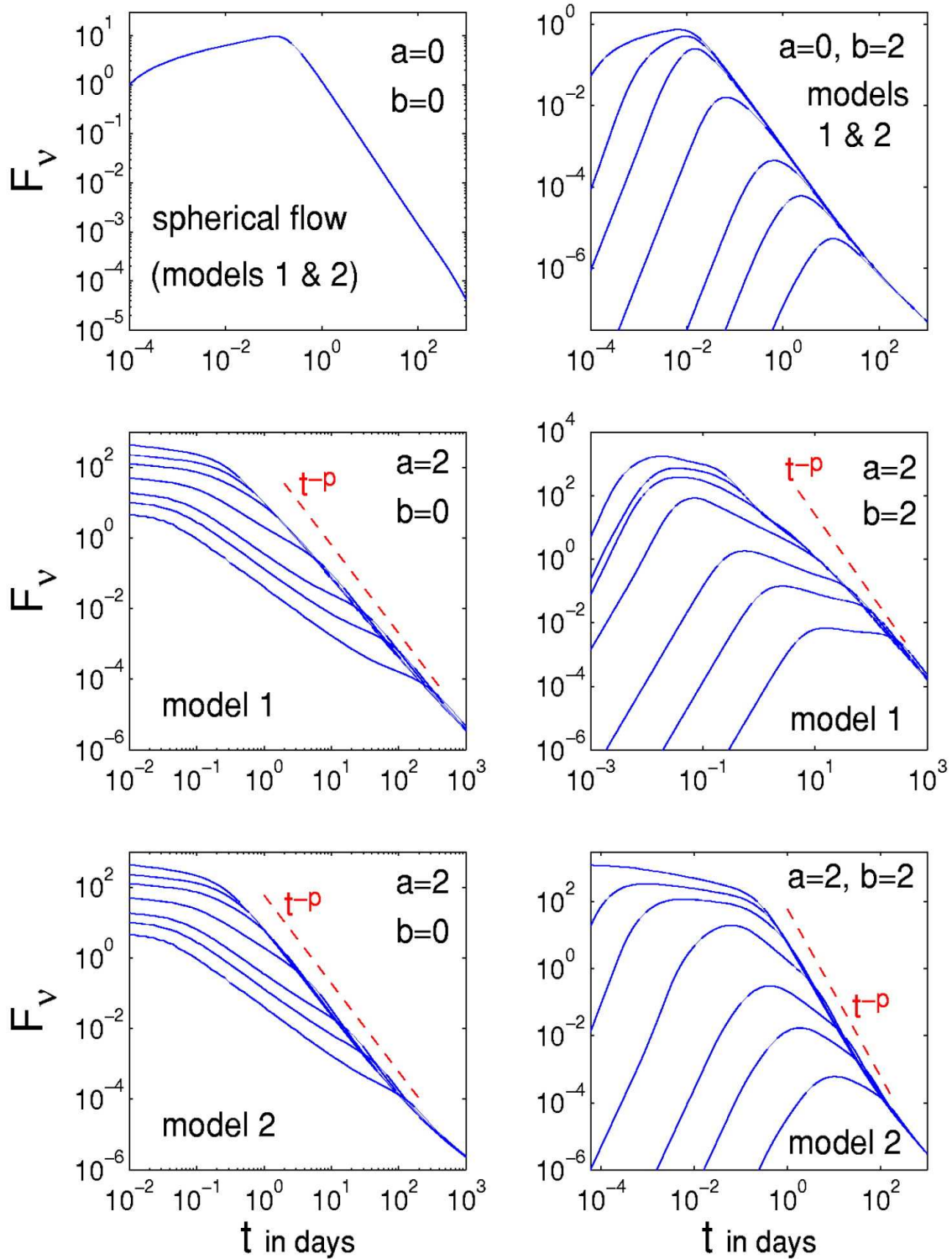
Figure 1.13: **Light curves from a Structured outflow :** Light curves for a constant-density external medium in the optical. A power-law of $t_{\oplus}^{-p}$ is added in some of the panels for comparison. Model 1 assumes that the energy per unit solid angle, ϵ does not change with time, $\epsilon(\theta, t) = \epsilon(\theta, t_0)$, while model 2 assumes the maximal averaging of ϵ over the angle a that is consistent with causality. See Granot and Kumar (2003) for the details of Model 1 and Model 2 from where this figure is taken.

- Apparent luminosities of GRBs in this model are different for different θ_v. The GRB luminosity function can be predicted and tested for different jet profiles. e.g. For the power-law model, $N(L)dL \propto L^{-1-2/a} \ dL$ and for Gaussian model, $N(L)dL \propto L^{-1} \ dL$ (Zhang and Mészáros, 2002a).

- The rate of burst detection as a function of observer angle (θ_v) can also be predicted in the structured jet model (Perna et al., 2003). e.g. For the a = 2 power-law model, a distribution peak is predicted around 0.12 rad, which is in rough agreement with the current data.

It should be noted that the Uniform Jet model has no prediction power on both these issues. Moreover, it is also interesting to note that some progenitor models naturally predicts outflows which have angular structure e.g. Poynting flux dominated outflow model by Lyutikov and Blandford (2002). For other studies see (Zhang et al., 2003; Barbiellini et al., 2003).

Criticism against the Structured Jet Models

Several criticisms directly against the structured jet model have been raised. The structured jet model with power-law angular profile requires a core of angle θ_c to avoid singularity along the jet axis. This is an unphysical assumption. But this assumption is not required for Gaussian jet profiles.

Some authors support the Uniform Jet model giving an argument that the Uniform Jet model is simpler and more realistic. According to them, different jet opening angles are naturally expected from physical processes and hence, are not surprising.

1.10.3 Orphan Afterglows

An interesting corollary of GRB collimation is Orphan afterglow, i.e. the afterglow for which GRB is not detected. If GRBs are indeed collimated then the GRBs and initially their afterglows would be visible only to *on-axis* observers which fall within the opening angle from the jet axis of the GRBs. As the collimated outflow decelerates and starts expanding sideways the opening angle of collimation widens and the afterglow becomes visible to the *off-axis* observers outside the initial opening angle from the jet axis. Thus the *off-axis* observers will see the afterglow even after having missed the GRB. Such orphan afterglows would be faint, difficult to detect and more importantly very hard to identify. Not surprisingly, none of them have been detected so far. Given this situation, the achromatic breaks remain the only practical tool to understand GRB collimation.

1.11 *Swift* Observations of Afterglows and the Unexplained Afterglow Behaviours

So far *Swift* have detected more than 200 GRBs and have followed up their afterglows, resulting in a rich collection of the x-ray afterglow behaviour, from a few tens of seconds after the burst up to about a month. This coverage also lead to discovery of some new features in the afterglows which were not predicted by the relativistic fireball model. To list a few of them :

- **Steep and shallow decay :** As described in § 1.2.1, the early part of the x-ray afterglow exhibit a sharp decline followed by a shallow decay. These are sometimes accompanied by the spectral evolution. To explain these features using the fireball model would require radical evolution of the spectral breaks. Instead, there have been attempts to explain these features using radiation

processes which are different from those responsible for the standard afterglow behaviour. A few notable explanations of the steep decay are the high latitude emission (Nousek et al., 2006; Zhang et al., 2006) and the radiation from the expanding cocoon surrounding the relativistic jet (Pe'er et al., 2006). As discussed in § 1.5, Zhang and Mészáros (2001, 2002) have proposed a model of energy injection to explain the shallow decay of the x-ray afterglows.

- **Sudden, bright flares :** The x-ray afterglows of some of the GRBs display bright flares. The total energy in some of these flares have been estimated to be comparable to the afterglow energies. King (2006) has proposed a different class of progenitors for the long GRBs – a NS-WD merger – in which such flares are expected to be seen.

- **Chromatic breaks :** The multi-band afterglows of many GRBs show chromatic breaks which are not accompanied by spectral evolution, ruling out passage of a spectral break through the waveband of observations as a reason for the break. There have been suggestions that the evolving microphysical parameters, i.e. $\epsilon_e \equiv \epsilon_e(t)$ and $\epsilon_B \equiv \epsilon_B(t)$, could be a possible reason for such breaks. Alternatively, the chromatic breaks in the afterglow light curves could be an indication that the optical and x-ray afterglows arise in different emitting regions (Panaitescu et al., 2006).

However, it should be noted that the plausible explanations given for the above mentioned behaviours of afterglows have not been tested against a large enough sample. In order to illustrate the perplexing behaviour of the afterglows, we give examples of two afterglows, GRB 050820a (Figure 1.14) and GRB 051109a (Figure 1.15).
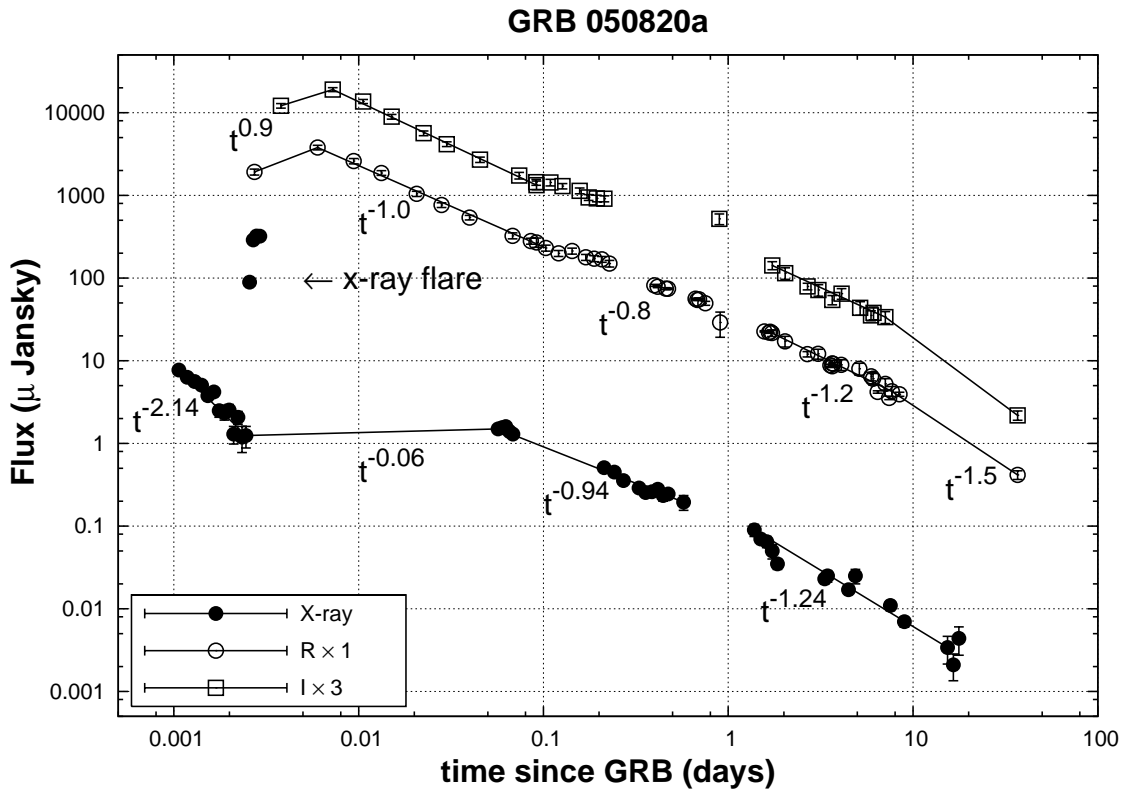
GRB 050820a

Figure 1.14: **Afterglow of GRB 050820a :** The solid lines are the best fit power-laws with the corresponding decay indices listed in the figure. The decay indices for the *I* and *R* band are similar within error. The time of GRB onset was taken to be UT 06:34:53 on 20 August 2005, which is the BAT trigger time. The x-ray and optical data is taken from Cenko et al. (2006) and Sahu et al. (2007). The early rise in the optical afterglow could be due to the passage of a spectral break v_m corresponding to the peak of the spectrum. We have tested the energy injection model (Zhang and Mészáros, 2001, 2002) with the luminosity of energy injection to be $L \propto t^{-q}$, by fitting the multiband afterglow and estimating the q parameter. If the optical and x-ray emissions arise in the same emitting regions then the q value for both the light curves should be same. We found that the q, for the flat decay of x-ray afterglow and the corresponding optical afterglow, to be inconsistent with each other which rules out the energy injection to be a correct description for the flat x-ray decay. However, we note that the q values for the subsequent x-ray decay with $\alpha \sim 0.94$ and the optical decay with $\alpha \sim 0.8$, to be marginally consistent with each other. The late break (at ~ 10 days) in the optical light curve has been interpreted by Cenko et al. (2006) as a jet break, however, there is no clear indication of the expected simultaneous break in the x-ray light curve.
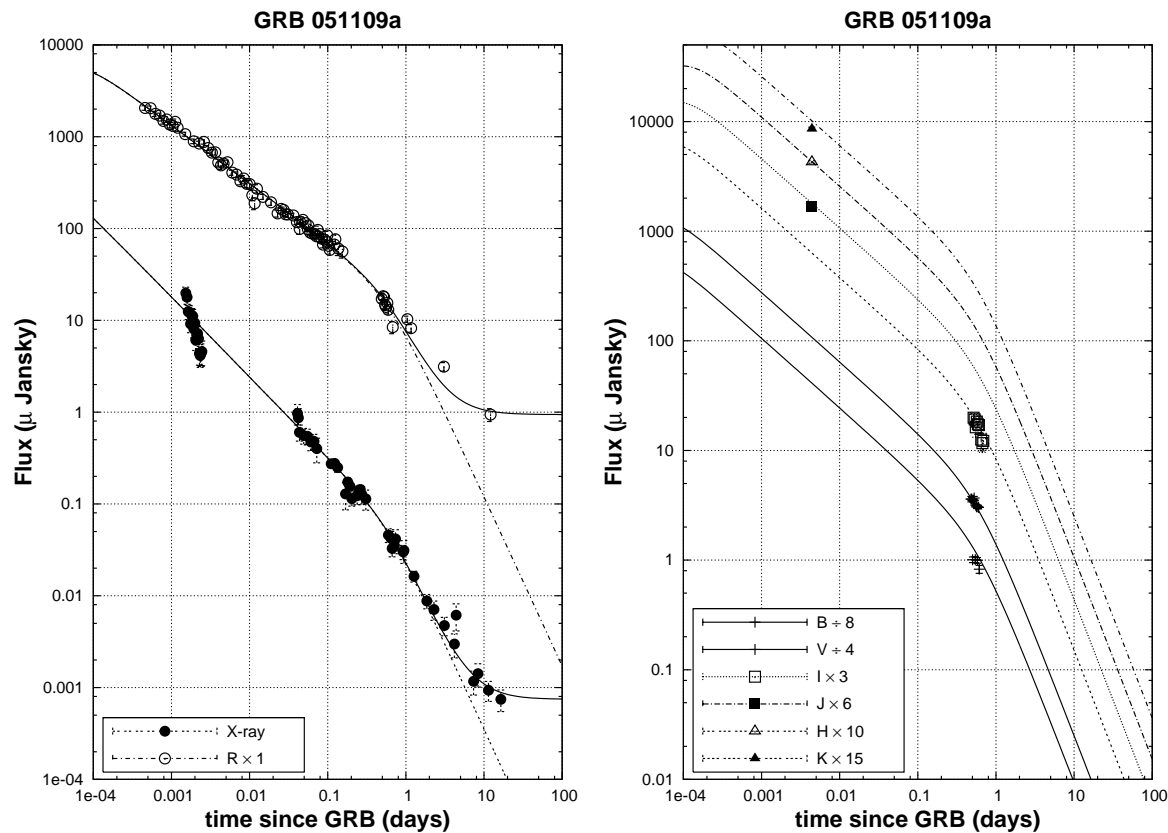
Figure 1.15: **Afterglow of GRB 051109a :** The lines represent the best fit model assuming that the optical and the x-ray emissions arise in the same emitting regions. The model assumes a jet break at ∼ 0.6 days after the burst and electron energy distribution index $p = 1.84$. It appears to be consistent with the rapid decline seen in B, V, I bands and the early part of the afterglow in J, H, K bands. However, the problems with this model in explaining the afterglow light curve are clearly visible when compared with the R band and x-ray light curves as shown in the left panel of this figure. Firstly, the observed post-break decays are inconsistent with the model predictions, especially at late times. To explain them, a constant flux contribution needs to be added to the light curve predicted by the model. The source, of such a constant flux in the optical could be the host galaxy of the GRB 051109a. However, a constant flux in x-rays would mean a nearby "galactic" source. Secondly, the present model predicts the x-ray afterglow which is brighter than that observed at early times. Under the present model it would be difficult to "hide" this afterglow contribution.

1.12   Organisation of the Thesis

The organisation of the thesis is as follows. In Chapter 2 we describe in detail the computer codes we have built to numerically model the multi-band afterglow light curves. In Chapter 3 we describe our observations of the afterglows and the telescopes and the detector systems used. The method of data analysis is elaborated in this chapter. During the course of this work, we have tried to detect the afterglows of various GRBs but not every attempt met with success. A complete list of GRBs for which we attempted to detect the afterglows is given in this chapter with the detailed log of observations as well as the upper limits obtained. Apart from this, the observations of the afterglows which were detected and followed up are listed in the corresponding chapters. Chapter 5 discusses the interesting case of GRB 050401 whose faint afterglow was detected in optical. The radio afterglow of GRB 030329 and our understanding of the non-relativistic phase of GRB fireball based on it is discussed in Chapter 4. Observations and modeling of GRB 050319 afterglow as being due to wind to ISM transition of the circum-burst medium, is discussed in Chapter 6. We present our conclusions and lessons learnt about the collimation in GRBs from the above mentioned studies, in Chapter 7.

Bibliography

Band D., Matteson J., Ford L. et al. ApJ, 413, 281 (1993).

Barbiellini G., Celotti A. and Longo F. MNRAS, 339, L17 (2003).

Berger E., Kulkarni S.R., Pooley G. et al. Nature, 426, 154 (2003).

Blandford R.D. and McKee C.F. Physics of Fluids, 19, 1130 (1976).

Bloom J.S., Frail D.A. and Kulkarni S.R. ApJ, 594, 674 (2003).

Cenko S.B., Kasliwal M., Harrison F.A. et al. ApJ, 652, 490 (2006).

Chevalier R.A. and Li Z.Y. ApJ, 536, 195 (2000).

Costa E., Frontera F., Heise J. et al. Nature, 387, 783 (1997).

Dai Z.G. and Gou L.J. ApJ, 552, 72 (2001).

Esin A.A. and Blandford R. ApJ Lett, 534, L151 (2000).

Frail D.A., Kulkarni S.R., Nicastro S.R., Feroci M. and Taylor G.B. Nature, 389, 261 (1997).

Frail D.A., Kulkarni S.R., Sari R. et al. ApJ Lett, 562, L55 (2001).

Frail D.A., Waxman E. and Kulkarni S.R. ApJ, 537, 191 (2000).

Fishman G.J. and Meegan C.A. ARA&A, 33, 415 (1995).

Galama T.J., Vreeswijk P.M., van Paradijs J. et al. A&AS, 138, 465 (1999).

Goodman J. New Astronomy, 2, 449 (1997).

Granot J. and Kumar P. ApJ, 591, 1086 (2003).

King A. proceedings of the Royal Society Scientific Discussion Meeting, London, September (2006).

Klebesadel R.W., Strong I.B. and Olson R.A. ApJ Lett, 182, L85+ (1973).

Kouveliotou C., Meegan C.A., Fishman G.J. et al. ApJ Lett, 413, L101 (1993).

Lithwick Y. and Sari R. ApJ, 555, 540 (2001).

Lyutikov M. and Blandford R. Ouyed R., (ed.) Beaming and Jets in Gamma Ray Bursts, 146–+ (2002).

Meegan C.A., Fishman G.J., Wilson R.B. et al. Nature, 355, 143 (1992).

Meszaros P. and Rees M.J. ApJ Lett, 418, L59+ (1993).

Meszaros P., Rees M.J. and Wijers R.A.M.J. ApJ, 499, 301 (1998).

Metzger M.R., Djorgovski S.G., Kulkarni S.R. et al. Nature, 387, 878 (1997).

Nousek J.A., Kouveliotou C., Grupe D. et al. ApJ, 642, 389 (2006).

Paciesas W.S. Baltic Astronomy, 13, 187 (2004).

Paciesas W.S., Meegan C.A., Pendleton G.N. et al. ApJS, 122, 465 (1999).

Paczynski B. and Rhoads J.E. ApJ Lett, 418, L5+ (1993).

Panaitescu A., Mészáros P., Burrows D. et al. MNRAS, 369, 2059 (2006).

Panaitescu A., Meszaros P. and Rees M.J. ApJ, 503, 314 (1998).

Pe'er A., Mészáros P. and Rees M.J. ApJ, 652, 482 (2006).

Perna R., Sari R. and Frail D. ApJ, 594, 379 (2003).

Rees M.J. and Meszaros P. MNRAS, 258, 41P (1992).

Rhoads J.E. ApJ Lett, 487, L1+ (1997).

Rhoads J.E. ApJ, 525, 737 (1999).

Rossi E., Lazzati D. and Rees M.J. MNRAS, 332, 945 (2002).

Ruderman M. New York Academy Sciences Annals, 262, 164 (1975).

Rybicki G.B. and Lightman A.P. Radiative Processes in Astrophysics (Radiative Processes in Astrophysics, by George B. Rybicki, Alan P. Lightman, pp. 400. ISBN 0-471-82759-2. Wiley-VCH , June 1986., 1986).

Sahu D., Kamble A., Parihar P., Bhat B. and Bhattacharya D. in preparation (2007).

Sari R., Piran T. and Narayan R. ApJ Lett, 497, L17+ (1998).

Usov V.V. Nature, 357, 472 (1992).

Usov V.V. MNRAS, 267, 1035 (1994).

van Paradijs J., Groot P.J., Galama T. et al. Nature, 386, 686 (1997).

Waxman E. and Draine B.T. ApJ, 537, 796 (2000).

Waxman E., Kulkarni S.R. and Frail D.A. ApJ, 497, 288 (1998).

Wijers R.A.M.J. and Galama T.J. ApJ, 523, 177 (1999).

Woosley S.E. ApJ, 405, 273 (1993).

Woosley S.E. and Bloom J.S. ARA&A, 44, 507 (2006).

Zhang B., Fan Y.Z., Dyks J. et al. ApJ, 642, 354 (2006).

Zhang B. and Mészáros P. ApJ Lett, 552, L35 (2001).

Zhang B. and Mészáros P. ApJ, 571, 876 (2002a).

Zhang B. and Mészáros P. ApJ, 566, 712 (2002b).

Zhang W., Woosley S.E. and MacFadyen A.I. ApJ, 586, 356 (2003).